

# 1 **Diagnosing spatial biases and uncertainties in global fire emissions** 2 **inventories: Indonesia as regional case study**

3 Tianjia Liu<sup>1</sup>, Loretta J. Mickley<sup>2</sup>, Miriam E. Marlier<sup>3</sup>, Ruth S. DeFries<sup>4</sup>, Md Firoz Khan<sup>5</sup>,  
4 Mohd Talib Latif<sup>6</sup>, and Alexandra Karambelas<sup>7</sup>

5 <sup>1</sup> Department of Earth and Planetary Sciences, Harvard University, Cambridge, MA, USA

6 <sup>2</sup> School of Engineering and Applied Sciences, Harvard University, Cambridge, MA, USA

7 <sup>3</sup> RAND Corporation, Santa Monica, CA, USA

8 <sup>4</sup> Department of Ecology, Evolution, and Environmental Biology, Columbia University, New York,  
9 NY, USA

10 <sup>5</sup> Department of Chemistry, Faculty of Science, University of Malaya, Kuala Lumpur, Malaysia

11 <sup>6</sup> School of Environmental and Natural Resource Sciences, Faculty of Science and Technology,  
12 Universiti Kebangsaan Malaysia, Bangi, Selangor, Malaysia

13 <sup>7</sup> The Earth Institute, Columbia University, New York, NY, USA

14 \*Corresponding Author: Tianjia Liu (tianjialiu@g.harvard.edu)

15 Keywords: fire emissions, MODIS, burned area, active fires, smoke, Indonesia, Google Earth Engine

## 16 **Abstract**

17 Models of atmospheric composition rely on fire emissions inventories to reconstruct and  
18 project impacts of biomass burning on air quality, public health, climate, ecosystem dynamics,  
19 and land-atmosphere exchanges. Many such global inventories use satellite measurements of  
20 active fires and/or burned area from the Moderate Resolution Imaging Spectroradiometer  
21 (MODIS). However, differences across inventories in the interpretation of satellite imagery, the  
22 emissions factors assumed for different components of smoke, and the adjustments made for  
23 small and obscured fires can result in large regional differences in fire emissions estimates across  
24 inventories. Using Google Earth Engine, we leverage 15 years (2003-2017) of MODIS  
25 observations and 6 years (2012-2017) of observations from the higher spatial resolution Visible  
26 Imaging Infrared Radiometer Suite (VIIRS) sensor to develop metrics to quantify five major  
27 sources of spatial bias or uncertainty in the inventories: (1) primary reliance on active fires  
28 versus burned area, (2) cloud/haze burden on the ability of satellites to “see” fires, (3)  
29 fragmentation of burned area, (4) roughness in topography, and (5) small fires, which are  
30 challenging to detect. Based on all these uncertainties, we devise comprehensive “relative fire  
31 confidence scores,” mapped globally at 0.25° x 0.25° spatial resolution over 2003-2017.

32 We then focus on fire activity in Indonesia as a case study to analyze how the choice of a  
33 fire emissions inventory affects model estimates of smoke-induced health impacts across  
34 Equatorial Asia. We use the adjoint of the GEOS-Chem chemical transport model and apply  
35 emissions of particulate organic carbon and black carbon (OC+BC smoke) from five global  
36 inventories: Global Fire Emissions Database (GFEDv4s), Fire Inventory from NCAR  
37 (FINNV1.5), Global Fire Assimilation System (GFASv1.2), Quick Fire Emissions Dataset  
38 (QFEDv2.5r1), and Fire Energetics and Emissions Research (FEERv1.0-G1.2). We find that  
39 modeled monthly smoke PM<sub>2.5</sub> in Singapore from 2003-2016 correlates with observed smoke  
40 PM<sub>2.5</sub>, with  $r$  ranging from 0.64-0.84 depending on the inventory. However, during the burning

41 season (July to October) of high fire years (e.g., 2006 and 2015), the magnitude of mean Jul-Oct  
42 modeled smoke  $PM_{2.5}$  can differ across inventories by more than  $20 \mu g m^{-3}$  ( $> 500\%$ ). Using the  
43 relative fire confidence metrics, we deduce that uncertainties in this region arise primarily from  
44 the small, fragmented fire landscape and very poor satellite observing conditions due to clouds  
45 and thick haze at this time of year. Indeed, we find that modeled smoke  $PM_{2.5}$  using GFASv1.2,  
46 which adjusts for fires obscured by clouds and thick haze and accounts for peatland emissions, is  
47 most consistent with observations in Singapore, as well as in Malaysia and Indonesia. Finally,  
48 we develop an online app called FIRECAM for end-users of global fire emissions inventories.  
49 The app diagnoses differences in emissions among the five inventories and gauges the relative  
50 uncertainty associated with satellite-observed fires on a regional basis.

## 51 **1. Introduction**

52 Models of atmospheric composition depend on global fire emissions inventories to  
53 reconstruct and project the impacts of biomass burning on air quality (Cusworth et al., 2018),  
54 public health (Crippa et al., 2016; Koplitz et al., 2016), climate (Rogers et al., 2015; Tosca et al.,  
55 2013), ecosystem dynamics (Yi et al., 2014), and land-atmosphere exchanges (Prentice et al.,  
56 2011). Many regional and global modeling studies consider only one global fire emissions  
57 inventory as input (Crippa et al., 2016; Hu et al., 2018; Kim et al., 2015; Koplitz et al., 2016;  
58 Maasakkers et al., 2016; Marlier et al., accepted) primarily to limit computational cost. End-users  
59 may simply choose an inventory based on spatio-temporal resolution, near-real-time availability,  
60 or keep the default inventory imposed in some chemical transport models (CTM). However,  
61 disagreements in the magnitude and temporal variability of emissions among inventories can  
62 significantly impact modeled estimates of variables relevant to air quality (Cusworth et al.,  
63 2018), public health (Koplitz et al., 2018), or the budgets of atmospheric species (Heymann et  
64 al., 2017; Li et al., 2019; Shi et al., 2015; Zhang et al., 2014). Thus, it is important to understand  
65 the underlying causes for differences in both the magnitude and spatio-temporal variability of  
66 fire emissions in order to better inform fire prediction (Chen et al., 2017), land management  
67 decisions (Marlier et al., accepted), and other applications. While previous studies have  
68 identified regional discrepancies among various global fire emissions inventories (e.g., Li et al.,  
69 2019; Shi et al., 2015), here we also construct metrics to diagnose such discrepancies, and we  
70 present the online app FIRECAM to allow end-users to rapidly compare inventories across the  
71 globe and view the metrics.

72 Five global fire emissions inventories are widely used in modeling studies: (1) Global  
73 Fire Emissions Database (GFED; van der Werf et al., 2017), (2) Fire Inventory from NCAR  
74 (FINN; Wiedinmyer et al., 2011), (3) Global Fire Assimilation System (GFAS; Kaiser et al.,  
75 2012), (4) Quick Fire Emissions Dataset (QFED; Darmenov and da Silva, 2013), and (5) Fire  
76 Energetics and Emissions Research (FEER; Ichoku and Ellison, 2014) (Table 1). Estimates of  
77 fire emissions generally follow the “bottom-up” (e.g. GFED, FINN) or “top-down” approach  
78 (e.g. QFED, GFAS, FEER). In this study, we broadly define “bottom-up” as burned area-based  
79 and “top-down” as fire energy-based. The bottom-up burned area approach in GFED and FINN  
80 is based on MODIS burned area (MCD64A1) and/or active fire (MOD14, MYD14) products. It  
81 is important to note that even the bottom-up approach relies on active fire data: GFED has  
82 essentially become a hybrid product that ingests active fire locations for its small fire boost  
83 (Randerson et al., 2012), and the MCD64A1 algorithm itself is coupled with active fire data  
84 (Giglio et al., 2009). Fuel loadings, combustion completeness, and emissions factors, which are

85 dependent on region and land use and land cover (LULC), are then used to convert burned area  
86 to fire emissions. Fuel loadings are derived from biogeochemical models (Hoelzemann et al.,  
87 2004; van der Werf et al., 2010), and combustion completeness is estimated as a function of soil  
88 moisture (van der Werf et al., 2017) or tree cover (Wiedinmyer et al., 2011). Emissions factors  
89 are compiled from lab experiments and vary by LULC (Akagi et al., 2011; Andreae and Merlet,  
90 2001). The top-down approach in QFED, GFAS, and FEER uses fire energy from MODIS-  
91 derived fire radiative power (FRP), which is remotely sensed at top-of-atmosphere. Fire radiative  
92 energy (FRE), or the temporal integral of FRP, approximately linearly scales with the mass of  
93 dry matter (DM) consumed as fuel due to combustion (Wooster et al., 2005). Besides correcting  
94 for fires obscured by clouds in the top-down approach, GFAS, QFED, and FEER also use  
95 MODIS aerosol optical depth (AOD) to determine scaling factors for emissions of organic  
96 carbon (OC), black carbon (BC), and particulate matter less than 2.5  $\mu\text{m}$  in diameter ( $\text{PM}_{2.5}$ ),  
97 which includes OC and BC (Darmenov and da Silva, 2013; Ichoku and Ellison, 2014; Kaiser et  
98 al., 2012).

99 To understand the causes for differences in fire emissions estimates, we first devise five  
100 “relative fire confidence metrics” based on major methodological differences between the five  
101 global inventories and factors that can affect satellite observing conditions: (1) type of input  
102 satellite fire dataset (i.e., burned area versus active fires), (2) cloud/haze obscuration of land  
103 surface, (3) burn extent and fragmentation, (4) variance in topography, and (5) additional small  
104 fires from VIIRS. We combine the five relative fire confidence metrics to map the relative fire  
105 confidence score for bottom-up emissions inventories primarily based on burned area (e.g.  
106 GFED) or active fire area (e.g. FINN). For top-down inventories, we estimate an FRP-based  
107 score to estimate the potential FRP enhancement from small fires below the MODIS detection  
108 limit, large fires not well-captured by the MODIS active fire product, and fires obscured by  
109 clouds and thick haze.

110 We then focus on Indonesia as a regional case study, as Indonesia can contribute a  
111 substantial fraction of annual global fire emissions. By some estimates, fires in Equatorial Asia,  
112 which mostly occur in Indonesia, account for 8% of carbon emissions from global fire activity on  
113 average, but as much as over a third during high fire years (van der Werf et al., 2017). From  
114 incomplete combustion, fires release greenhouse gases and aerosols, including  $\text{PM}_{2.5}$ , and such  
115 emissions can trigger haze events, impacting visibility, air quality, climate, ecosystem services,  
116 and human health (Harrison et al., 2009; Page et al., 2009). Three main factors exacerbate haze  
117 episodes over Equatorial Asia: (1) synoptic meteorology, (2) fire-driven deforestation and  
118 agricultural management, and (3) carbon-rich peatlands in Indonesia. First, during years with a  
119 strong El Niño and positive Indian Ocean Dipole phase, such as 2006 and 2015, suppression of  
120 convection over Indonesia leads to drought conditions (Crippa et al., 2016; Fernandes et al.,  
121 2017; Koplitz et al., 2016). Chen et al. (2017) found a temporal cascade of pan-tropical fires,  
122 including large fires in Indonesia, driven by the El Niño Southern Oscillation (ENSO) and  
123 modulated by changes in precipitation and terrestrial water storage. Second, smallholder farms  
124 and industrial concessions (oil palm, pulpwood, and rubber) are typically managed by fire  
125 (“slash and burn”) to clear residues; forests are also cleared for agriculture and new plantations  
126 via burning (Dennis et al., 2005; Hoscilo et al., 2011; Marlier et al., 2015). Third, if the water  
127 table is low, peat fires can burrow underground and become extremely difficult to extinguish.  
128 Such fires can smolder for days to weeks, releasing substantial amounts of smoke into the

129 atmosphere (Gras and Jensen, 1999; Hayasaka et al., 2014; Rein et al., 2008; van der Werf et al.,  
130 2008).

131 The high concentrations of PM<sub>2.5</sub> generated by fires in Equatorial Asia pose adverse  
132 health risks, leading to increased premature mortality. For example, Koplitz et al. (2016), Crippa  
133 et al. (2016), and Marlier et al. (accepted) estimate 75,600-100,300 long-term premature adult  
134 deaths from cardiovascular and respiratory disease in Equatorial Asia due to the 2015 severe  
135 haze event. However, each of these studies differ in methodology, and specifically, in the global  
136 fire emissions inventory used: GFASv1.0 in Koplitz et al. (2016), FINNv2.0 in Crippa et al.  
137 (2016), and GFEDv4s in Marlier et al. (accepted). In this study, we diagnose the impact of using  
138 different emissions inventories on estimates of population-weighted smoke exposures for  
139 Singapore, Indonesia, and Malaysia, following Koplitz et al. (2016) and Marlier et al. (accepted).

140 To summarize, we first identify the methodological differences between five global fire  
141 emissions inventories and use Google Earth Engine (GEE) to develop five relative fire  
142 confidence metrics to quantify some of the uncertainties. GEE is an online platform that couples  
143 a multi-petabyte-scale data catalog with cloud computing to make rapid geospatial analysis  
144 possible on a global scale (Gorelick et al., 2017). Next, we isolate the impact of using different  
145 inventories to estimate smoke exposure in Equatorial Asia from fires in Indonesia. Finally, we  
146 develop an online tool to help end-users to rapidly gauge the regional differences in emissions  
147 estimates and reduce potential biases in model results.

## 148 **2. Methods**

### 149 *2.1 Satellite fire datasets*

150 We leverage GEE to access, process, and analyze the satellite datasets needed for this  
151 study, as described below. We primarily use the Collection 6 (C6) satellite fire datasets from the  
152 MODIS sensors aboard the Terra and Aqua satellites, which have daily overpasses at ~10:30  
153 am/pm and ~1:30 am/pm local time, respectively. These datasets are used in the construction of  
154 the five global fire emissions inventories considered here. We analyze 15 years (2003-2017) of  
155 data from Collection 6 MCD64A1 burned area at monthly, 500-m spatial resolution (Giglio et  
156 al., 2018, 2009), MOD/MYD14A1 FRP and fire mask at daily, 1-km resolution (Giglio et al.,  
157 2016, 2003), and MCD14ML active fire geolocations also at daily, 1-km resolution. We  
158 hereafter refer to the Level-3 gridded active fire products MOD14A1 (Terra) and MYD14A1  
159 (Aqua) collectively as MxD14A1 and Level-2 swath products as MxD14. We also use Collection  
160 1 VNP14IMGML active fire geolocations, available since 2012, from the VIIRS sensor aboard  
161 the Suomi National Polar-orbiting Partnership (S-NPP) satellite. VNP14IMGML is analogous to  
162 MCD14ML, but provides data at higher spatial resolution (375 m) and only during the Aqua  
163 overpass times (Schroeder and Giglio, 2017). All MODIS and VIIRS datasets are available from  
164 the NASA Earthdata catalog (<https://earthdata.nasa.gov/>).

### 165 *2.2 Relative fire confidence metrics*

166 We devise five simple fire confidence metrics ( $\phi$ ) to assess the overall spatial variability  
167 and relative bias in global fire emissions inventories at 0.25° x 0.25° spatial resolution and  
168 aggregated across 15 years (2003-2017) from monthly timesteps, as described below. Then, as an  
169 example to end-users, we integrate the five metrics into more comprehensive “scores” to

170 independently evaluate the spatial variability in uncertainty for bottom-up and top-down  
171 inventories. That is, we identify regions where each inventory may capture fire emissions either  
172 well or poorly, based on the five metrics.

173 **(1) Spatial discrepancy between burned area and active fire area ( $\phi_{area}$ ):** We classify two  
174 main types of bottom-up emissions inventories, based on the observations used to derive these  
175 inventories. For example, both GFED and FINN estimate burned area, but GFED uses the  
176 MCD64A1 burned area product, and FINN relies on MCD14ML active fire geolocations.  
177 MODIS burned area is typically classified based on the difference in the surface reflectance, or  
178 Normalized Burn Ratio (NBR), of pre-burn and post-burn images, while MODIS active fires are  
179 detected as “hotspots,” or thermal anomalies, each of which can be associated with areal extent  
180 to estimate burned area. To avoid confusion, we refer to burned area derived from MCD64A1 as  
181  $BA_{MCD64A1}$  or burned area (BA; as in GFED) and that from MxD14A1 as  $BA_{MxD14A1}$  or “active  
182 fire area” (AFA; as in FINN). In contrast to the high threshold for the MCD64A1 burned area  
183 product, which reliably classifies burn scars  $> 1.2 \text{ km}^2$  (Giglio et al., 2006), the MxD14A1 active  
184 fire product can detect cool, smoldering fires more consistently and fires as small as  $100 \text{ m}^2$   
185 under clear-sky conditions (Giglio et al., 2003). However, burned area products may better  
186 capture short-lasting fires and fires obscured by thick haze or clouds since the burned area pre-  
187 burn versus post-burn algorithm is not limited by satellite overpass times (Giglio et al., 2009). To  
188 gauge the relative areal discrepancy of  $BA_{MCD64A1}$  and  $BA_{MxD14A1}$ , we first aggregate  
189  $BA_{MCD64A1}$  to the 1-km spatial resolution of  $BA_{MxD14A1}$ . We then estimate total  $BA_{MCD64A1}$   
190 outside  $BA_{MxD14A1}$  ( $BA_\beta$ ) and  $BA_{MxD14A1}$  outside  $BA_{MCD64A1}$  ( $BA_\alpha$ ), over 2003-2017, and  
191 calculate the normalized difference index of  $BA_\beta$  and  $BA_\alpha$  at  $0.25^\circ \times 0.25^\circ$  spatial resolution:

$$192 \quad \phi_{area} = \frac{\Sigma BA_\beta - \Sigma BA_\alpha}{\Sigma BA_\beta + \Sigma BA_\alpha} \quad (1)$$

193 where

$$194 \quad BA_\beta = BA_{MCD64A1} - (BA_{MCD64A1} \cap BA_{MxD14A1}) \quad (2)$$

$$195 \quad BA_\alpha = BA_{MxD14A1} - (BA_{MCD64A1} \cap BA_{MxD14A1}) \quad (3)$$

196 The range of the normalized difference index (-1 to +1) for the BA-AFA discrepancy indicates  
197 whether grid cells are either dominated by burned area ( $> 0$ ) or active fire area ( $< 0$ ). If either  
198 burned area or active fire area dominates (near -1 or +1), the datasets will not agree, and  
199 uncertainty is high. If the index is  $\sim 0$ , the discrepancies between the datasets are minimal,  
200 wherein  $BA_\beta \approx BA_\alpha$ ; in this case, however, the magnitude of  $BA_\beta$  and  $BA_\alpha$  can vary while  
201 yielding similar index values.

202 **(2) Cloud/haze effect on the ability of satellites to “see” fires ( $\phi_{cloud\_haze}$ ):** Persistent cloud  
203 coverage and thick haze limit the opportunities for satellites to detect active fires or retrieve  
204 usable scenes for burned area classification. This metric diagnoses the fractional monthly  
205 cloud/haze burden at 500-m spatial resolution, weighted by FRP. We use FRP rather than burned  
206 area since FRP is linearly related to DM emissions and more readily captures small fires  
207 (Wooster et al., 2005). We use the Collection 6 MODIS daily surface reflectance products  
208 MxD09GA and follow the algorithm proposed by Xiang et al. (2013) in each pixel, with “pixel”  
209 defined as one satellite observation in the native MODIS sinusoidal projection:

210 
$$p_{cloud\_haze} = \frac{\rho_7 - \rho_1}{\rho_7 + \rho_1} < 0 \text{ or } \rho_1 > 0.3 \quad (4)$$

211 where  $p_{cloud\_haze}$  refers to pixels designated as cloudy/hazy,  $\rho_1$  indicates the MODIS surface  
212 reflectance in the 620-670 nm band (Red) and  $\rho_7$ , the 2105-2155 nm band (SWIR-2). Cloudy and  
213 hazy pixels tend to be saturated in the visible bands relative to SWIR bands (Xiang et al., 2013).  
214 Pixels are classified as cloudy/hazy if either of the two criteria is met (Eq. 4). We consider only  
215 those pixels with one or more active fire or burned area observations over the 2003-2017  
216 timeframe to exclude misclassification of cloud/haze in snow, ice, and desert regions. After  
217 averaging the fraction of clouds and haze across  $0.25^\circ \times 0.25^\circ$  grid cells, we weight the monthly  
218 fractional cloud/haze burden by FRP aggregated by month and satellite, over 2003-2017, to place  
219 more emphasis on the observing conditions during the months and hours of the diurnal cycle  
220 when fires are more likely to occur.

221 Like Xiang et al. (2013), MODIS also diagnoses clouds and haze but at coarser, 1-km  
222 resolution, which can result in overestimates of the cloud/haze fraction since clear pixels are  
223 mixed with cloudy or mixed cloudy pixels. However, the MODIS algorithm is better able than  
224 Xiang et al. (2013) to separate clouds or haze from bright surfaces such as snow/ice, desert, and  
225 built-up areas. We therefore use the FRP-weighted cloud/haze fraction derived from the MODIS  
226 algorithm to identify grid cells that may be misclassified as clouds due to the underlying bright  
227 surfaces. We assume that those pixels that MODIS characterizes as “cloudy” or having “mixed”  
228 clouds, cloud shadow, or high aerosol content are pixels obscured by cloud or haze. Then, for  
229 these grid cells, we check whether the FRP-weighted cloud/haze fraction derived from the Xiang  
230 et al. (2013) algorithm is positive. If yes, we use the FRP-weighted cloud/haze fraction from the  
231 MODIS algorithm for our metric.

232 **(3) Fragmentation and size of contiguous burned area ( $\phi_{fragment}$ ):** Burned area products can  
233 better capture large, contiguous fires than small, fragmented fires due to the greater difference in  
234 NBR from pre-fire to post-fire and the persistence of burn scars on the land surface. On  
235 croplands, the small drop in NBR due to small fires can be conflated with harvest or masked by  
236 timely sowing of the next crop or by regrowth (e.g. Hall et al., 2016; Liu et al., 2019). In  
237 contrast, active fire products can generally detect such small, fragmented fires more accurately,  
238 so long as they occur during the satellite overpasses and are not obscured by clouds or haze.  
239 Dense clusters of small fires within a pixel can also increase the detection probability by  
240 enhancing the thermal anomaly or the NBR difference relative to background. For this metric,  
241 we estimate the total burned area and number of burn scar fragments over 2003-2017, using the  
242 average burned area per contiguous burn scar patch as a proxy for burn scar size and  
243 fragmentation. The *connectedComponents* function in GEE allows us to estimate the number of  
244 contiguous burn patches on a monthly basis at 500-m spatial resolution (Gorelick et al., 2017).  
245 To determine the connectivity of burn scars, we apply a circle kernel with a radius of 1 pixel; this  
246 assumes a “half neighbors” scheme, in which each pixel has 4 neighbors, and only pixels that  
247 share an edge are merged. One limitation of *connectedComponents* is that the algorithm limits  
248 the maximum number of pixels per patch at 256 pixels and identifies larger patches as  
249 background. We account for this limitation by increasing the total number of burn scar fragments  
250 in a grid cell by one if the MCD64A1 burned area is larger than the size of the patch derived by  
251 *connectedComponents*. Additionally, the  $0.25^\circ \times 0.25^\circ$  grid used to extract the contiguous burn  
252 scars sets an upper bound on burned area per patch for those large fires extending across multiple

253 grid cells. Values  $> 2 \text{ km}^2$  per burn fragment indicate large, contiguous fires, while small values  
254 represent small, fragmented fires.

255 **(4) Roughness in topography ( $\phi_{topography}$ ):** Rough terrain, or large variances in local  
256 elevation, can inhibit active fire detection or burned area classification by introducing shadows,  
257 leading to insufficient background control pixels and artificial variations in surface reflectance  
258 (Fornacca et al., 2017). We estimate the neighborhood variance of terrain elevation as an  
259 indication of rough terrain. We use the U.S. Geological Survey (USGS) Global Multi-resolution  
260 Terrain Elevation Data 2010 (GMTED2010) at 7.5 arc seconds ( $\sim 250 \text{ m}$ ) spatial resolution,  
261 derived primarily from the Shuttle Radar Topography Mission (SRTM) Digital Terrain Elevation  
262 Data from the National Geospatial-Intelligence Agency (NGA). For each pixel, we estimate the  
263 neighborhood variance using a square kernel with a radius of 2 pixels. We then mask out water  
264 bodies using the 250-m MODIS/Terra land/water mask (MOD44W C6) and upscale the  
265 topography variance to  $0.25^\circ \times 0.25^\circ$  spatial resolution by calculating the mean. Values close to  
266 0 indicate flat topography, while values  $> 1000 \text{ m}^2$  indicate rough, mountainous terrain.

267 **(5) Additional small fires detected by VIIRS ( $\phi_{VIIRS_{sf}}$ ):** VIIRS aboard S-NPP detects active  
268 fires at 375-m (I-bands) and 750-m (M-bands) spatial resolution in comparison to the 1-km  
269 spatial resolution of MODIS active fire detections (Schroeder and Giglio, 2017). The difference  
270 in spatial resolution suggests that VIIRS can detect smaller and cooler fires than MODIS.  
271 However, global fire emissions inventories have historically depended on MODIS since VIIRS is  
272 available only since 2012, or over a decade less than MODIS. While these additional small fires  
273 may comprise only a small portion of the global carbon budget, they can be important local point  
274 sources that contribute to regional air pollution. We approximate additional FRP observed by  
275 VIIRS at 375-m spatial resolution as the fractional FRP of VIIRS fires outside MODIS active  
276 fire and burned area pixels during the time period when the two satellite records overlap (2012-  
277 2017). Values range from 0 (no additional VIIRS FRP outside MODIS burn extent) to 1 (only  
278 VIIRS FRP).

### 279 *2.2.1 Bottom-up inventories: relative fire confidence scores (BA-score, AFA-score)*

280 Taken together, the five metrics described above capture the primary reliance on MODIS  
281 burned area (e.g., GFED) versus active fire (e.g., FINN) products as the base input satellite-  
282 derived fire dataset in a bottom-up approach and difficulty in the satellite detection of fires due to  
283 cloud/haze obscuration and limited spatial and temporal resolution. Using these five metrics, we  
284 estimate a relative fire confidence score for the two bottom-up emissions inventories, which are  
285 based on either burned area (as in GFED) or active fire area (as in FINN). For each metric and  
286 each grid cell, we assign an initial integer confidence score ranging from 0 to 10, with 10 as  
287 highest confidence score, based on the decile distribution of all grid cells. Grid cells with only  
288 MODIS active fire, only MODIS burned area, or only VIIRS active fire observations are  
289 assigned the lowest confidence score of 0. We then average the scores from the fire confidence  
290 metrics in each grid cell and re-center the scale by setting the median score for the final relative  
291 fire confidence score for that grid cell to 0. This score represents the relative degree to which we  
292 can be confident in fire emissions for these inventories. We associate low cloud/haze burden, low  
293 variance in elevation, and low fraction of additional VIIRS fires with high confidence. To assess  
294 inventories based on burned area (e.g., GFED), we calculate a “BA-score,” in which high burned  
295 area outside active fire area (metric 1) and low burn fragmentation (metric 3) denote high  
296 confidence. For inventories based on active fires (e.g., FINN), we calculate an “AFA-score,” in

297 which we reverse the scales for metrics 1 and 3 and place more relative confidence in grid cells  
298 dominated by active fire area over burned area and fragmented burn landscapes.

### 299 *2.2.2 Top-down inventories: adjusted potential FRP adjustment (pFRP)*

300 Top-down FRP-based inventories often include statistical cloud-gap adjustment and/or  
301 smoke AOD constraints, making them difficult to directly compare against the bottom-up  
302 inventories. Cloud-gap adjustments correct for fires blocked from satellite detection due to  
303 clouds or thick haze. These adjustments rely on data assimilation of previous observations and  
304 assumptions regarding fire persistence (Darmenov and da Silva, 2013; Kaiser et al., 2012). As an  
305 additional top-down constraint, fire emissions are scaled to match smoke-aerosol emissions  
306 derived from AOD observations (Ichoku and Ellison, 2014). We thus devise a separate score, the  
307 adjusted potential FRP enhancement (pFRP), or “FRP-score,” to assess the three top-down  
308 inventories (GFAS, QFED, FEER). The pFRP score diagnoses additional fire energy,  
309 unaccounted for by the MODIS active fires product but indicated by large burn scars from the  
310 MODIS burned area product or very small fires from the 375-m VIIRS active fires product. We  
311 first estimate the potential FRP enhancement as the sum of (1) fractional FRP inside MCD64A1  
312 burned area extent but outside active fire area, over 2003-2017, and (2) fractional VIIRS FRP  
313 outside the combined extent of both MODIS burned area and active fire area, or metric 5, over  
314 2012-2017. To obtain the adjusted potential FRP enhancement, we then multiply the potential  
315 FRP enhancement by the complement of the cloud/haze obscuration fraction, or metric 2. High  
316 pFRP values suggest low confidence in top-down inventories under clear-sky conditions.

### 317 *2.3 Global fire emissions inventories*

318 To convert burned area or FRP into emissions, fire emission inventories rely on estimates  
319 and assumptions regarding an array of variables as land cover type, fuel load, or emissions  
320 factors. Here we summarize these estimates and assumptions across five inventories (GFEDv4s,  
321 FINNv1.5, GFASv1.2, QFEDv2.5r1, and FEERv1.0-G1.2) over 2003-2016 and at both global  
322 and regional scale (Table 1). The versions of the inventories considered here are current as of  
323 2018. We then compare the resulting emissions of carbon dioxide (CO<sub>2</sub>), carbon monoxide (CO),  
324 methane (CH<sub>4</sub>), OC, BC, and PM<sub>2.5</sub> emissions from five global fire emissions inventories. Each  
325 inventory is described in more detail in Supplementary Section S2.

### 326 *2.4 Modeling smoke PM<sub>2.5</sub> from regional fire emissions*

327 Following Kim et al. (2015) and Koplitz et al. (2016), we use the adjoint of the GEOS-  
328 Chem CTM to estimate the influence of upwind fires on smoke exposure at population-weighted  
329 receptors. We define smoke PM<sub>2.5</sub> as the enhancement in PM<sub>2.5</sub> due to fire activity. As used here,  
330 the GEOS-Chem adjoint maps the sensitivities of smoke PM<sub>2.5</sub> at particular receptors to fire  
331 emissions in grid cells across a source region, creating a footprint of such sensitivities. These  
332 footprints depend on the transport pathways from the source to the receptor and vary with  
333 meteorology. By multiplying these sensitivities by the different fire emissions inventories, we  
334 can easily compare estimates of monthly smoke PM<sub>2.5</sub> exposure in Indonesia, Singapore, and  
335 Malaysia, from 2003-2016. We thus apply monthly adjoint sensitivities, which span a range of  
336 meteorology from 2005-2009, to the sum of OC and BC emissions, the main components of  
337 smoke PM<sub>2.5</sub>. Due to the high computational cost of the GEOS-Chem adjoint, we match existing  
338 2005-2009 sensitivities to each emissions year from 2003-2016 by determining the closest



339 meteorological year in terms of rainfall (Kim et al., 2015; Koplitz et al., 2016). To do so, we use  
340 daily rainfall rates from Climate Hazards Group Infrared Precipitation with Station Data  
341 (CHIRPS; Funk et al., 2015), averaged temporally over the fire season and spatially over  
342 Sumatra and Kalimantan, Indonesia (Figure S3). As in Fernandes et al. (2017) and Marlier et al.  
343 (accepted), we define the fire season in Indonesia as July to October.

344 Following Marlier et al. (accepted), we further validate modeled smoke  $PM_{2.5}$  with  
345 ground observations in Singapore. We first extend the daily  $PM_{2.5}$  observations, available from  
346 2014-2016, from the Singapore National Environment Agency (NEA) to 2010 by converting  
347 Pollution Standards Index (PSI) observations to  $PM_{2.5}$ . As used by the Singapore NEA, PSI is an  
348 air quality index that incorporates concentrations of six pollutants: CO, sulfur dioxide ( $SO_2$ ),  
349 nitrogen dioxide ( $NO_2$ ), ozone ( $O_3$ ),  $PM_{10}$ , and  $PM_{2.5}$  (<https://www.haze.gov.sg/>). To further  
350 extend the record back to 2003, we train a multi-variate regression model of monthly mean NEA  
351  $PM_{2.5}$  observations using visibility, air temperature, wind speed, and rainfall observations from  
352 the Singapore Changi airport, available from NOAA Global Summary of the Day (GSOD). The  
353 model yields an adjusted  $r^2$  with observations of 0.94 (Figure S5). We then reconstruct monthly  
354  $PM_{2.5}$  for 2003-2016 and subtract the background  $PM_{2.5}$ , or the median  $PM_{2.5}$  ( $13.77 \mu g m^{-3}$ )  
355 during non-fire season months (January to June and November to December), to obtain smoke  
356  $PM_{2.5}$  for our validation. Validation for Malaysia and Indonesia is described in Supplementary  
357 Section S3.2.

## 358 **4. Results**

### 359 *4.1 Spatial patterns in relative fire confidence metrics and scores*

360 Overall, the five relative fire confidence metrics broadly differentiate: (1) large,  
361 continuous versus small, fragmented landscapes, (2) cloudy/hazy versus clear satellite observing  
362 conditions during the fire season, and (3) flat versus mountainous or rugged terrain. First, the  
363 map of BA-AFA discrepancies (metric 1) reveals the regions where the burned area  $BA_\beta$  and  
364 active fire area extent  $BA_\alpha$  disagree. Regions dominated by high burned area outside the active  
365 fire area extent ( $BA_\beta \gg BA_\alpha$ ) include the western Australia shrublands, sub-Saharan Africa  
366 savannas, and Kazakhstan and eastern Mongolia grasslands. Regions dominated by active fire  
367 area outside burned area extent ( $BA_\beta \ll BA_\alpha$ ) are more widespread and primarily cover  
368 agricultural and/or mountainous areas (Figure 1). Additionally, this metric highlights artificial  
369 discontinuities in the MODIS burned area product, most prominently north of the Black Sea,  
370 likely due to separate data processing for each MODIS tile (Giglio et al., 2018). Second, the  
371 FRP-weighted cloud/haze fraction (metric 2) shows that tropical and boreal forest regions, as  
372 well as eastern China, are conducive to poor satellite observing conditions due to cloud or haze  
373 during the fire season, with index values greater than 0.5 (Figure 2). These areas with persistent  
374 cloud/haze burden are consistent with independent estimates of high mean cloud frequency  
375 (Wilson and Jetz, 2016) and are also co-located with high MODIS burn date uncertainty,  
376 indicating that many retrieved satellite scenes are unusable (Figure S9). Third, the pattern of burn  
377 size and fragmentation (metric 3) is similar to that of the BA-AFA discrepancy: areas with large,  
378 contiguous fires are better captured by burned area, while areas with small, fragmented fires are  
379 better represented by active fire detections (Figure 3). Our method for burn size/fragmentation  
380 yields spatial patterns consistent with fire size from the Global Fire Atlas, a catalog that

381 characterizes over 13 million individual fires detected by MODIS (Andela et al., 2019). Fourth,  
382 topographical variance (metric 4) differentiates mountainous or rugged terrain, such as in  
383 western U.S. and southeast Asia, versus flat terrain, such as in northern India and western  
384 Australia (Figure 4). Fifth, the map of VIIRS fires outside the MODIS burn extent (metric 5)  
385 reveals locations dominated by small fires that are not well-detected by a coarser resolution  
386 sensor like MODIS (Figure 5). In total, 38% of total VIIRS FRP does not overlap with the  
387 MODIS burn extent, revealing the importance of very small fires.

388 Taken together, the five metrics compose the relative fire confidence scores for bottom-  
389 up emissions inventories primarily derived from either burned area (BA-score; Figure S1a), such  
390 as GFEDv4s, or active fire area (AFA-score; Figure S1b), such as FINNv1.5. While the mapped  
391 BA-score and AFA-score mostly track the patterns of the large, contiguous fires versus small,  
392 fragmented fires, some areas exhibit low relative confidence (e.g., eastern China croplands,  
393 Democratic Republic of Congo tropical forests) or high relative confidence (e.g., central-  
394 southern Amazon forests, southern Africa savannas in Botswana and Namibia) for both scores  
395 due to the effects of cloud/haze cover and/or topographical variance. Some caveats apply here.  
396 While we take the BA-score to apply to GFEDv4s, this inventory also boosts burned area using  
397 active fire counts to account for small fires. Additionally, for AFA-score, we assume an active  
398 fire area of 1 km<sup>2</sup> for all fires, while FINNv1.5 uses 0.75 km<sup>2</sup> for savanna and grassland fires and  
399 further scales the active fire area for all fires by the fractional vegetation cover of a given 1-km  
400 pixel (Wiedinmyer et al., 2011). Both GFEDv4s and FINNv1.5 rely on outdated MODIS  
401 products: GFEDv4s on MCD64A1 C5.1 burned area and FINNv1.5 on MCD14DL C5 active  
402 fires; however, for all our metrics, we use updated satellite products from MODIS C6  
403 (MCD64A1 and MxD14A1). Despite our simplified approach and use of different versions of the  
404 satellite fire products, the normalized difference between GFEDv4s burned area and FINNv1.5  
405 active fire area is spatially well-correlated with the BA-AFA discrepancy ( $r = 0.59, p < 0.01$ ), or  
406 metric 1. We also find that the normalized difference between GFEDv4s and FINNv1.5  
407 emissions for all six species is also moderately correlated with the BA-AFA discrepancy ( $r =$   
408  $0.53-0.57, p < 0.01$ ), confirming that the difference between GFEDv4s and FINNv1.5 emissions  
409 is related to the satellite fire input dataset used.

410 The pFRP metric assesses top-down FRP-based emissions inventories (GFAS, QFED,  
411 and FEER; Figure S2). In total, we estimate 24% and 38% potential FRP enhancement from  
412 large fires (using MODIS BA) and very small fires (using VIIRS FRP), respectively, from 2003-  
413 2017. Put another way, the FRP-based inventories may be missing nearly two-thirds of fires  
414 under clear-sky conditions. Regions with low pFRP, and thus high uncertainty, include India and  
415 sub-Saharan Africa. In these regions, the low pFRP implies that either the satellite overpasses are  
416 missing a large number of short-lived or fast-spreading fires or the fires are too small to detect at  
417 coarse resolution. For example, the satellite overpasses at 10:30 am and 1:30 pm likely  
418 underestimate fire energy in the sub-tropics, where fire activity generally peak in the late  
419 afternoon (Giglio, 2007). Regions characterized by high cloud/haze cover during the fire season,  
420 such as tropical and boreal forests, have low pFRP due to our assumption that the cloud-gap  
421 corrections in these inventories successfully capture the fires obscured by clouds/haze.

#### 422 *4.2 Comparison of global fire emissions inventories: speciation and emissions factors*

423 We find inconsistencies in the speciation of the overall emissions budget for CO<sub>2</sub>, CO,  
424 CH<sub>4</sub>, OC, BC, and PM<sub>2.5</sub> across the five global fire emissions inventories. For example,

425 QFEDv2.5r1 and FEERv1.0-G1.2 estimate ~2-3 times as much OC, BC, and PM<sub>2.5</sub> emissions  
426 than the other inventories, with QFEDv2.5r1 higher than FEERv1.0-G1.2 (Table 2). Mean  
427 annual OC + BC emissions, from 2003-2016, among inventories differ by 5-126% in coefficient  
428 of variation (CV; Figure 6). In regions with a high CV, such as temperate North America (102%)  
429 and the Middle East (126%), QFEDv2.5r1 OC+BC emissions are much higher than those from  
430 other inventories. These discrepancies shed light on the impact of the different algorithms that  
431 convert burned area or fire energy into aerosol emissions. For example, QFED and FEER apply  
432 top-down constraints on aerosol emissions to match smoke AOD, while such adjustments are  
433 absent in GFED, FINN, and GFAS. FEER uses smoke AOD to directly calculate TPM, which is  
434 then broken down into aerosol species, while QFED enhances aerosol emissions with a constant  
435 global scaling factor for each LULC (Darmenov and da Silva, 2013; Ichoku and Ellison, 2014).  
436 This global, rather than regional, AOD-based scaling in QFED may explain the large CV in the  
437 Middle East and North America. Indeed, using MODIS/Aqua AOD, Darmenov and da Silva  
438 (2013) find significant variation in these scaling factors across each LULC – e.g., from 2-3 in  
439 tropical forest, 3-5 in extratropical forests, and 1-3 in grasslands and savannas.

440 To better understand the discrepancies across inventory emissions, we examine the  
441 emissions factors used in GFEDv4s and in earlier versions of FINN, GFAS, and QFED:  
442 FINNv1.0, GFASv1.0, and QFEDv2.4. We assume that emissions factors for the current versions  
443 of these three inventories do not deviate significantly from those in previous versions (Darmenov  
444 and da Silva, 2013; Kaiser et al., 2012; Wiedinmyer et al., 2011). First, we assess the impact of  
445 LULC classification on emissions factors by deriving a globally averaged emissions factor for  
446 each emitted species in each inventory, weighted by the total DM emissions for each LULC. To  
447 isolate the differences in LULC classification among inventories, we use the GFEDv4s DM  
448 emissions partitioned by LULC for the weighting. Since FINN subdivides the GFEDv4s savanna,  
449 grasslands, and shrublands LULC into two smaller LULC, we derive weights for these LULC  
450 using FINNv1.5 emissions. We find that the coefficients of variation in emission factors across  
451 the four inventories are relatively small for CO<sub>2</sub>, CO, OC, and BC (1.75-6.67%), compared to  
452 those for CH<sub>4</sub> and PM<sub>2.5</sub> (20.3-26.7%; Table 3). On average, GFEDv4s and GFAS, which  
453 consider peatlands as a separate LULC, have about 60% higher weighted mean emissions factors  
454 for CH<sub>4</sub> than FINN and QFED. This discrepancy arises because the peat emissions factor (20.8 g  
455 CH<sub>4</sub> kg<sup>-1</sup> DM) is ~2.5-14 times as high as CH<sub>4</sub> emissions factors for other LULC (Table S1), and  
456 only GFEDv4s and GFAS consider peatlands separately. In contrast to Li et al. (2019), we do not  
457 consider that FEERv1.0-G1.2 accounts for peatlands (Table 1), since FEER only uses the  
458 “permanent wetland” classification from the MODIS land cover product, which misses much of  
459 the peatland cover in Indonesia compared to the Olson et al. (2001) dataset used by GFED (van  
460 der Werf et al., 2017) and GFAS (Heil et al., 2010; Kaiser et al., 2012). The high CH<sub>4</sub>, as well as  
461 CO, emissions factors for peat fires can be attributed to incomplete combustion from smoldering  
462 fires, which are common in boreal and tropical peatlands (Kasischke and Bruhwiler, 2002;  
463 Stockwell et al., 2016). Additionally, the PM<sub>2.5</sub> emissions factors used in FINN for woody  
464 savanna/shrubland and savanna/grassland (8.3-15.4 g PM<sub>2.5</sub> kg<sup>-1</sup> DM) are 16-214% higher than  
465 those used in GFEDv4s, GFAS, QFED (4.9-7.17 g PM<sub>2.5</sub> kg<sup>-1</sup> DM) for the broader savanna,  
466 grassland, and shrubland LULC, which may explain the high PM<sub>2.5</sub> weighted mean emissions  
467 factor for FINN (Table S1).

#### 468 4.3 Modeling monthly smoke $PM_{2.5}$ from Indonesia fires

469 We use monthly GEOS-Chem adjoint sensitivities, from 2005-2009, with the five global  
470 fire emissions inventories to model smoke  $PM_{2.5}$  in Singapore, Malaysia, and Indonesia from  
471 2003-2016, focusing on the impact of upwind Indonesian fires (Figure 7-8, S7-8). According to  
472 GFEDv4s, peat fires contributed almost half of total OC+BC emissions in Indonesia from 1997-  
473 2016. Modeled monthly mean smoke  $PM_{2.5}$  is moderately to strongly correlated with  
474 observations ( $r = 0.64$  to  $0.84$ ,  $p < 0.01$ ), with GFASv1.2 smoke  $PM_{2.5}$  most closely matching the  
475 temporal variability of observed  $PM_{2.5}$  enhancement from smoke (Figure 8a). We find similarly  
476 strong correlations for population-weighted smoke  $PM_{10}$  in Malaysia ( $r = 0.54$  to  $0.89$ ,  $p < 0.01$ )  
477 and satellite AOD in Indonesia ( $r = 0.63$  to  $0.93$ ,  $p < 0.01$ ; Figures S7-S8). While the correlation  
478 of modeled and observed smoke  $PM_{2.5}$  in Singapore is consistent across inventories, the  
479 magnitude of modeled smoke  $PM_{2.5}$  can differ by more than  $20 \mu\text{g m}^{-3}$  for the Jul-Oct average  
480 during extreme smoke episodes, such as in 2006 and 2015 (Figure 8b). For example, the models  
481 yield mean Jul-Oct smoke  $PM_{2.5}$  concentrations in 2006 that differ from observed smoke by -  
482 64% to +70%. For the 2006, 2009, and 2015 high fire years, modeled Jul-Oct smoke  $PM_{2.5}$  using  
483 GFASv1.2 yields the smallest mean absolute error relative to the observations (16%), compared  
484 to such errors from the other four inventories (39-66%).

##### 485 4.3.1. 2006 and 2015 severe haze events

486 Using GFASv1.0 and the GEOS-Chem adjoint, Koplitz et al. (2016) estimate over 150%  
487 higher premature mortality in Equatorial Asia in 2015 (100,300 excess deaths) than in 2006  
488 (37,600 excess deaths). This suggests higher exposure to smoke and more prolonged fire activity,  
489 as well as drier El Niño conditions, in 2015 compared to 2006. We first compare relative changes  
490 in modeled Jul-Oct mean smoke exposure in Singapore between the 2006 and 2015 fire seasons.  
491 In addition, the strong negative exponential relationship between rainfall and metrics of fire  
492 activity (e.g., active fire count, burned area) in Indonesia is well-established (Fernandes et al.,  
493 2017; van der Werf et al., 2017). However, Cusworth et al. (2018) suggest that thick haze may  
494 obscure fires from satellite detection. To determine whether fire activity in Equatorial Asia is  
495 under-detected in 2015 due to haze, we first model the linear relationship between rainfall and  
496 fire activity, as well as with satellite AOD, in the log-log space for the 2003-2016 period. We use  
497 Jul-Oct rainfall rates from CHIRPS and MxD08\_M3 AOD. As measures of seasonal mean fire  
498 activity, we use the MxD14A1 active fire mask, MxD14A1 FRP, and MCD64A1 burned area,  
499 averaged over the Indonesian provinces of Sumatra and Kalimantan, where most fires are  
500 concentrated. We then predict 2015 fires in the context of the log-log linear regression of rainfall  
501 and fires, modeled excluding 2015 observations. If fires are under-detected due to haze in 2015,  
502 then active fire counts, FRP, and burned area should deviate negatively from the modeled log-log  
503 rainfall-fire relationships, compared to AOD, which should not deviate significantly.

504 Several phenomena indicate a more severe haze episode in 2015 than in 2006. The Niño  
505 3.4 index, which is a proxy for ENSO and based on anomalies in tropical Pacific sea surface  
506 temperatures, suggests a stronger El Niño in 2015 than in 2006 (Koplitz et al., 2016). In addition,  
507 lower rainfall rates (-29%) and higher AOD (+31-34%) over Sumatra and Kalimantan in 2015  
508 suggest drier and hazier conditions over these fire-prone regions, relative to 2006. In contrast,  
509 minimal increases in active fire count (+6%) and FRP (+10%) in 2015 relative to the long-term  
510 MODIS record, and even decreases in burned area (-35%) suggest that increased haziness in  
511 2015 may have obscured many fires, making satellite detection of fires challenging. During the

512 Indonesia fire season (Jul-Oct), satellite-observed smoke AOD and indicators of fire activity  
513 strongly correlate with rainfall in log-log space over 2003-2016 when 2015 is excluded ( $r = -0.87$   
514 to  $-0.98$ ,  $p < 0.01$ ; Figure 9). Given these relationships with rainfall, the 2015 fire activity  
515 appears severely underestimated, with active fire 60% less than expected, burned area 93% less,  
516 and FRP 62% less. In contrast, AOD in 2015 does not deviate significantly ( $-12\%$ ) from the  
517 modeled log-log relationship with rainfall.

518 The observed AOD and FRP in 2015 are within the 95% prediction interval for these  
519 variables, but burned area and active fire counts are outside this interval. We now examine how  
520 these potential underestimates in 2015 fire activity may have affected the fire emissions  
521 inventories. We find that GFEDv4s, which includes a small fires boost, and FINNv1.5, which  
522 uses active fires to estimate burned area, less severely underestimate (63-76%) burned area in  
523 2015 than the MODIS burned area product (Figure S4). Inventories that make cloud-gap  
524 adjustments for obscured fires are better able to discern the more severe haze event in 2015 and  
525 match the observed enhancement of 183% in smoke  $PM_{2.5}$  in Singapore: GFASv1.2 shows a  
526 155% increase in smoke  $PM_{2.5}$  relative to 2006, and QFEDv2.5r1 and FEERv1.0-G1.2 yield  
527 increases of 96-137% (Figure 8b). In contrast, GFEDv4s and FINNv1.5 do not capture the  
528 enhanced smoke  $PM_{2.5}$  in Singapore in 2015. Overall, GFASv1.2 most accurately captures both  
529 the magnitude and temporal variability of observed smoke  $PM_{2.5}$ , while FINNv1.5 consistently  
530 underestimates smoke  $PM_{2.5}$  in high fire years and most poorly captures the temporal variability  
531 of observed smoke  $PM_{2.5}$ .

## 532 **5. Discussion and Conclusions**

### 533 *5.1 Relative fire confidence metrics: spatial patterns*

534 The goal of this study has been to quantify and interpret differences across five bottom-  
535 up and top-down global fire emission inventories. While it is difficult to directly compare  
536 bottom-up and top-down inventories, end-users may use the relative confidence indicated by the  
537 BA-score, AFA-score, and FRP-score (pFRP) to select a “best” inventory if limited by  
538 computing resources or assess the five relative fire confidence metrics individually. One  
539 important limitation is that the relative fire confidence metrics are time-averaged and therefore  
540 do not fully account for interannual or seasonal variability in fire activity. However, in  
541 constructing these metrics, we have placed greater weight on high fire years and the dominant  
542 fire-prone months in order for end-users to diagnose the overall spatial biases among inventories.  
543 Another caveat is that we do not investigate in as much detail the spatial differences in  
544 inventory-specific LULC, which affect the fuel consumption and emissions factors imposed.

545 We first find that two fire landscapes – large and cohesive versus small and fragmented –  
546 account for broad differences in the bottom-up fire emissions inventories, GFED and FINN.  
547 GFED, which relies primarily on observed burned area, better captures emissions from large,  
548 cohesive fires, while FINN, which depends on observed active fires, better diagnoses emissions  
549 from small, fragmented fires. Second, the presence of thick cloud/haze during peak fire activity  
550 makes satellite fire detection more difficult in equatorial regions, boreal regions, and eastern  
551 China. Third, fires located in mountainous regions are also challenging to detect, especially by  
552 moderate-resolution sensors, such as MODIS (500 m or 1 km) or VIIRS (375 m or 750 m). For  
553 top-down fire emissions inventories (e.g., GFAS, QFED, and FEER), we calculate a pFRP score,  
554 which indicates potential underestimates in FRP under clear-sky conditions. We find high pFRP

555 scores suggest that areas dominated by fast-spreading, large fires or short-lived, small fires under  
556 clear-sky conditions are not well-captured by MODIS due to limited overpasses or moderate  
557 spatial resolution.

## 558 *5.2 Regional application: validation of modeled smoke PM<sub>2.5</sub> across Equatorial Asia from* 559 *Indonesia fires*

560 Here we discuss the application of the relative fire confidence metrics for Indonesia fires.  
561 (Additional examples for the contiguous United States and northwestern India are discussed in  
562 Supplementary Section S6.) We can first deduce that fire-prone regions in Indonesia generally  
563 follow the small, fragmented fire landscape pattern (metrics 1, 3, and 5) and that high cloud  
564 cover and/or haze (metric 2) may impede observation during the fire season. While metric 4  
565 shows rough terrain in parts of Indonesia (e.g., western Sumatra, Java, and northern Kalimantan),  
566 most fires occur on flat terrain. However, smoldering peat fires even on flat land may also be  
567 difficult to detect.

568 First, we find that thick haze in very high fire years, such as 2015, likely leads to lower-  
569 than-expected fire activity derived from satellite observations. The AFA-score suggests high  
570 relative confidence for FINN, in contrast to the low relative confidence by BA-score for GFED;  
571 pFRP shows low potential FRP enhancement over Indonesia, primarily because of the presence  
572 of thick clouds or haze. Our results suggest that the 93% burned area underestimate in Indonesia  
573 arises primarily due to thick haze, an effect greater than the effect of such haze on active fire  
574 count (-60%) or FRP (-62%). For Singapore, as well as for Malaysia and Indonesia, we find that  
575 top-down inventories yield modeled smoke PM<sub>2.5</sub> concentrations that are more consistent with  
576 observed PM<sub>2.5</sub> than bottom-up inventories, with  $r = 0.78-0.84$  for top-down versus  $r = 0.64-0.73$   
577 for bottom-up inventories. This result is likely due to the cloud-gap adjustments in the top-down  
578 inventories.

579 Second, only GFAS and GFED consider peatlands as a separate LULC, while in other  
580 inventories, peatlands may be classified as savanna, tropical forest, or cropland. These  
581 discrepancies have implications for emissions since the carbon-rich peatlands are associated with  
582 high fuel load (van der Werf et al., 2010). While the moderate to strong correlation of observed  
583 and modeled smoke PM<sub>2.5</sub> is consistent across inventories, the magnitude of mean Jul-Oct smoke  
584 PM<sub>2.5</sub> in the high fire years of 2006 and 2015 can vary by more than 20  $\mu\text{g m}^{-3}$ , with GFEDv4s  
585 and GFASv1.2 best capturing the magnitude of observed smoke PM<sub>2.5</sub> and yielding higher  
586 smoke PM<sub>2.5</sub> than the other three inventories. Additionally, estimated ratios of peat OC/BC  
587 emissions factors ratios are  $\sim 150$  compared to just 3-39 for other LULC types, thereby affecting  
588 the composition of smoke PM<sub>2.5</sub>. Indeed, GFEDv4s and GFASv1.2 show 78-380% higher Jul-  
589 Oct OC/BC ratios over Sumatra and Kalimantan during 2003-2016 than the other three  
590 inventories. In summary, GFASv1.2, which adjusts for cloud gaps in satellite observations of  
591 fires and considers peatlands as a separate LULC class, performs best in terms of modeling  
592 smoke PM<sub>2.5</sub> that is consistent with observations in both temporal variability and magnitude.

## 593 *5.3 Uncertainties in global fire emissions inventories*

594 The uncertainties in global fire emissions inventories influence estimates of emissions  
595 budgets, the spatio-temporal variability of fires, and fire trends, with different inventories leading  
596 to different conclusions (Supplementary Section S7). Here we discuss the main sources of  
597 uncertainty in inventories: small fires, cloud gap adjustments, aerosol emissions enhancements,

598 and emissions factors and LULC classification. Sole reliance on burned area from MCD64A1  
599 may capture large, contiguous fires well but not the spatial allocation of small fires in fragmented  
600 burn landscapes. This is demonstrated by the moderate spatial correlation ( $r = 0.36$ ,  $p < 0.01$ )  
601 between the BA-AFA discrepancy (metric 1) and burn size/fragmentation (metric 3). Additional  
602 VIIRS FRP detected outside the MODIS active fire extent (metric 5) also implies low confidence  
603 in areas dominated by small fires. As an example of low confidence in small fires, we find that  
604 many grid cells in GFEDv4s would not have any emissions without the small fires boost.  
605 Approximately one-fourth of grid cells with nonzero GFEDv4s fire emissions from 2003-2016  
606 persistently show 100% spatial coverage by small fires, and the small fire boost alone contributes  
607 all the emissions in 57% of GFEDv4s grid cells, on average. Zhang et al. (2018) recommended  
608 that grid cells with only small fire contribution, or no MCD64A1 burned area input, be treated  
609 with caution. For example, these authors found that GFEDv4s significantly overestimates DM  
610 fuel consumption and emissions for areas with infrequent but small fires in eastern China during  
611 summer months. Under such conditions, when no burned area is detected, the scaling parameters  
612 applied to the total active fire count are not specific to individual grid cells and instead are  
613 averaged across regions, seasons, and land cover types (van der Werf et al., 2017).

614 On the other hand, because MODIS retrieves thermal anomalies only during satellite  
615 overpass times, use of MCD14ML active fires in the bottom-up inventories, as well as MxD14  
616 FRP in the top-down inventories, may lead to underestimates of burned area and fire energy from  
617 large, contiguous fires. In addition, the FINN emissions inventory may overrepresent small fire  
618 emissions due to the assumption that at least 75% of the nominal pixel area is burned  
619 (Wiedinmyer et al., 2011). The active fire product also has coarser resolution and a lower  
620 detection threshold compared to the burned area product. Using FRP may address this  
621 overestimate since small fires are cooler and exhibit lower FRP. Nonetheless, the dependence of  
622 the top-down inventories on GFED to convert FRP to DM burned may lead to underestimates of  
623 small fire emissions, as seen in the case of agricultural fire emissions in northwestern India  
624 (Cusworth et al., 2018).

625 The cloud/haze fraction (metric 2) indicates that regions with persistent cloud cover or  
626 thick haze during the fire season, such as boreal and tropical regions, degrade the quality of  
627 satellite observations of fire activity. By adjusting for cloud gaps and scaling with observed  
628 AOD, the top-down inventories – GFASv1.2, QFEDv2.5r1 and FEERv1.0-G1.2 – may be better  
629 able to match observations than the bottom-up inventories in these regions (Kopplitz et al., 2018).  
630 However, the scaling factor of 3.4 recommended by Kaiser et al. (2012) for GFAS aerosol  
631 emissions, as well as the simple global QFED scaling by LULC, may bias regional smoke  
632 exposure estimates (e.g., Kopplitz et al., 2016) due to spatial variations in AOD scaling  
633 (Darmenov and da Silva, 2013; Ichoku and Ellison, 2014). We thus recommend comparison of  
634 aerosol emissions from QFEDv2.5r1 to FEERv1.0-G1.2, which directly estimates TPM using  
635 smoke AOD by region. Further, QFED calibrates the coefficient  $\beta$  relating FRP to DM globally,  
636 while GFAS uses LULC-specific  $\beta$  coefficients, which vary from 0.13 to 5.87 kg DM MJ<sup>-1</sup> FRP  
637 (Kaiser et al., 2012). We also show that certain species, such as CH<sub>4</sub>, are greatly affected by  
638 LULC classification within the inventories, and in particular, by the treatment of peatland  
639 emissions. In our case study of Indonesian fires, GFEDv4s and GFASv1.2, both of which  
640 account for peatlands, yield much higher smoke PM<sub>2.5</sub> more in line with observations than the  
641 other three inventories. Finally, coarse-resolution LULC maps (0.5°-1°), which are used in

642 GFASv1.2 and FEERv1.0-G1.2, may also bias emissions due to differences in fuel loadings in  
643 regions with more heterogenous LULC, such as in Southeast Asia (Figure S10b).

#### 644 *5.4 Future directions and recommendations*

645 Integration of both burned area and active fire products into fire emission inventories  
646 may reduce underestimation of fires in small and fragmented or large and contiguous fire  
647 regions, respectively. Similar to the hybrid approach of using active fires for the small fire boost  
648 in GFEDv4s, incorporation of burned area in FINN could retroactively improve emissions  
649 estimates for large fires. For the top-down inventories of GFAS, QFED, and FEER, use of  
650 burned area as a secondary input satellite fire dataset may yield emissions more closely matched  
651 with observations compared to the current dependence on assumptions of fire persistence across  
652 cloud gaps and satellite overpasses. Standardization of emissions factors, in particular in the  
653 partitioning of LULC, could help reduce inconsistencies between inventories. In particular, the  
654 peatland maps used, if any, are incomplete and could be improved using more comprehensive  
655 global peatland datasets, such as PEATMAP (Xu et al., 2018). We also expect that the updated  
656 MODIS MCD12Q1 land cover dataset from C5 to C6 will lead to some differences between  
657 current and future emissions estimates (Sulla-Menashe et al., 2019). Further, access to high  
658 spatial resolution surface reflectance datasets from Landsat (30 m, every 16 days) and Sentinel-2  
659 (20 m, every 5 days) in the GEE data catalog makes feasible both ground truth validation and  
660 improvement of burned area estimates and LULC classifications (Casu et al., 2017). Recent  
661 studies have shown overall improvement in accuracy and small burn scar detection using  
662 Landsat and Sentinel, but low revisit times may limit this improvement in areas with high  
663 cloudiness and rapid land use change (Crowley et al., 2019; Goodwin and Collett, 2014;  
664 Hawbaker et al., 2017; Roteta et al., 2019).

665 For end-users, we recommend use of multiple bottom-up and top-down inventories, if  
666 possible. Further, end-users should be aware that outdated emissions estimates can persist in  
667 models, leading to biases and errors in model results (Supplementary Section S8). We present  
668 here an online tool, “Fire Inventories: Regional Evaluation, Comparison, and Metrics”  
669 (FIRECAM; <https://globalfires.earthengine.app/view/firecam>), that allows users to compare  
670 regional monthly and yearly emissions, from 2003-2016, from the five global inventories for six  
671 species (CO, CO<sub>2</sub>, CH<sub>4</sub>, OC, BC, and PM<sub>2.5</sub>) and to interpret the regional differences between  
672 fire emissions by using the five relative fire confidence metrics (Figure S11, Supplementary  
673 Section S5). FIRECAM will be updated regularly in the foreseeable future as new versions of the  
674 inventories and underlying datasets become available. We identify three key factors that should  
675 influence the end-user’s inventory selection and can also significantly affect the results of  
676 modeling studies: input satellite fire dataset, statistical adjustments, and LULC classification and  
677 emissions factors. For example, in our case study on Indonesian fires, we find that the cloud-gap  
678 adjustment and representation of peatland emissions are two important factors that distinguish  
679 different inventories in the regional validation of smoke PM<sub>2.5</sub>; both factors are included in the  
680 GFAS inventory. FIRECAM allows users to rapidly assess such differences in regional fire  
681 emissions.

#### 682 **Code Availability**

683 Code for the FIRECAM tool can be accessed from <https://github.com/tianjialiu/FIRECAM>.



## 684 **Acknowledgements**

685 T. Liu is funded by a NSF Graduate Research Fellowship (NSF grant DGE1745303). We  
686 acknowledge the Singapore National Environment Agency (NEA) and Malaysian Department of  
687 Environment (DOE) for maintaining a network of stations that provide continuous air quality  
688 measurements across Singapore and Malaysia.

## 689 **References**

- 690 Akagi, S.K., Yokelson, R.J., Wiedinmyer, C., Alvarado, M.J., Reid, J.S., Karl, T., Crounse, J.D.,  
691 Wennberg, P.O., 2011. Emission factors for open and domestic biomass burning for use in  
692 atmospheric models. *Atmos. Chem. Phys.* 11, 4039–4072. [https://doi.org/10.5194/acp-11-](https://doi.org/10.5194/acp-11-4039-2011)  
693 4039-2011
- 694 Andela, N., Morton, D.C., Giglio, L., Paugam, R., Chen, Y., Hantson, S., van der Werf, G.R.,  
695 Randerson, J.T., 2019. The Global Fire Atlas of individual fire size, duration, speed, and  
696 direction. *Earth Syst. Sci. Data* 11, 529–552. <https://doi.org/10.5194/essd-2018-89>
- 697 Andreae, M.O., Merlet, P., 2001. Emissions of trace gases and aerosols from biomass burning.  
698 *Global Biogeochem. Cycles* 15, 955–966. <https://doi.org/10.1029/2000GB001382>
- 699 Casu, F., Manunta, M., Agram, P.S., Crippen, R.E., 2017. Big Remotely Sensed Data: tools,  
700 applications and experiences. *Remote Sens. Environ.* 202, 1–2.  
701 <https://doi.org/10.1016/j.rse.2017.09.013>
- 702 Chen, Y., Morton, D.C., Andela, N., van der Werf, G.R., Giglio, L., Randerson, J.T., 2017. A  
703 pan-tropical cascade of fire driven by El Niño/Southern Oscillation. *Nat. Clim. Chang.* 7,  
704 906–911. <https://doi.org/10.1038/s41558-017-0014-8>
- 705 Crippa, P., Castruccio, S., Archer-Nicholls, S., Lebron, G.B., Kuwata, M., Thota, A., Sumin, S.,  
706 Butt, E., Wiedinmyer, C., Spracklen, D. V., 2016. Population exposure to hazardous air  
707 quality due to the 2015 fires in Equatorial Asia. *Sci. Rep.* 6, 1–9.  
708 <https://doi.org/10.1038/srep37074>
- 709 Crowley, M.A., Cardille, J.A., White, J.C., Wulder, M.A., 2019. Multi-sensor, multi-scale,  
710 Bayesian data synthesis for mapping within-year wildfire progression. *Remote Sens. Lett.*  
711 10, 302–311. <https://doi.org/10.1080/2150704x.2018.1536300>
- 712 Cusworth, D.H., Mickley, L.J., Sulprizio, M.P., Liu, T., Marlier, M.E., DeFries, R.S.,  
713 Guttikunda, S.K., Gupta, P., 2018. Quantifying the influence of agricultural fires in  
714 northwest India on urban air pollution in Delhi, India. *Environ. Res. Lett.* 13, 044018.  
715 <https://doi.org/10.1088/1748-9326/aab303>
- 716 Darmenov, A.S., da Silva, A., 2013. The Quick Fire Emissions Dataset (QFED) - Documentation  
717 of versions 2.1, 2.2, and 2.4, NASA Technical Report Series on Global Modeling and Data  
718 Assimilation, Volume 32.
- 719 Dennis, R.A., Mayer, J., Applegate, G., Chokkalingam, U., Colfer, C.J.P., Kurniawan, I.,  
720 Lachowski, H., Maus, P., Permana, R.P., Ruchiat, Y., Stolle, F., Suyanto, Tomich, T.P.,  
721 2005. Fire, people and pixels: Linking social science and remote sensing to understand  
722 underlying causes and impacts of fires in Indonesia. *Hum. Ecol.* 33, 465–504.  
723 <https://doi.org/10.1007/s10745-005-5156-z>

- 724 Fernandes, K., Verchot, L., Baethgen, W., Gutierrez-Velez, V., Pinedo-Vasquez, M., Martius,  
725 C., 2017. Heightened fire probability in Indonesia in non-drought conditions: the effect of  
726 increasing temperatures. *Environ. Res. Lett.* 12, 054002. <https://doi.org/10.1088/1748-9326/aa6884>  
727
- 728 Fornacca, D., Ren, G., Xiao, W., 2017. Performance of Three MODIS fire products (MCD45A1,  
729 MCD64A1, MCD14ML), and ESA Fire\_CCI in a mountainous area of Northwest Yunnan,  
730 China, characterized by frequent small fires. *Remote Sens.* 9, 1131.  
731 <https://doi.org/10.3390/rs9111131>
- 732 Funk, C., Peterson, P., Landsfeld, M., Pedreros, D., Verdin, J., Shukla, S., Husak, G., Rowland,  
733 J., Harrison, L., Hoell, A., Michaelsen, J., 2015. The climate hazards infrared precipitation  
734 with stations - A new environmental record for monitoring extremes. *Sci. Data* 2, 1–21.  
735 <https://doi.org/10.1038/sdata.2015.66>
- 736 Giglio, L., 2007. Characterization of the tropical diurnal fire cycle using VIRS and MODIS  
737 observations. *Remote Sens. Environ.* 108, 407–421.  
738 <https://doi.org/10.1016/j.rse.2006.11.018>
- 739 Giglio, L., Boschetti, L., Roy, D.P., Humber, M.L., Justice, C.O., 2018. The Collection 6  
740 MODIS burned area mapping algorithm and product. *Remote Sens. Environ.* 217, 72–85.  
741 <https://doi.org/10.1016/j.rse.2018.08.005>
- 742 Giglio, L., Csiszar, I., Justice, C.O., 2006. Global distribution and seasonality of active fires as  
743 observed with the Terra and Aqua Moderate Resolution Imaging Spectroradiometer  
744 (MODIS) sensors. *J. Geophys. Res. Biogeosciences* 111, 1–12.  
745 <https://doi.org/10.1029/2005JG000142>
- 746 Giglio, L., Descloitres, J., Justice, C.O., Kaufman, Y.J., 2003. An enhanced contextual fire  
747 detection algorithm for MODIS. *Remote Sens. Environ.* 87, 273–282.  
748 [https://doi.org/10.1016/S0034-4257\(03\)00184-6](https://doi.org/10.1016/S0034-4257(03)00184-6)
- 749 Giglio, L., Loboda, T., Roy, D.P., Quayle, B., Justice, C.O., 2009. An active-fire based burned  
750 area mapping algorithm for the MODIS sensor. *Remote Sens. Environ.* 113, 408–420.  
751 <https://doi.org/10.1016/j.rse.2008.10.006>
- 752 Giglio, L., Schroeder, W., Justice, C.O., 2016. The collection 6 MODIS active fire detection  
753 algorithm and fire products. *Remote Sens. Environ.* 178, 31–41.  
754 <https://doi.org/10.1016/j.rse.2016.02.054>
- 755 Goodwin, N.R., Collett, L.J., 2014. Development of an automated method for mapping fire  
756 history captured in Landsat TM and ETM+ time series across Queensland, Australia.  
757 *Remote Sens. Environ.* 148, 206–221. <https://doi.org/10.1016/j.rse.2014.03.021>
- 758 Gorelick, N., Hancher, M., Dixon, M., Ilyushchenko, S., Thau, D., Moore, R., 2017. Google  
759 Earth Engine: Planetary-scale geospatial analysis for everyone. *Remote Sens. Environ.* 202,  
760 18–27. <https://doi.org/10.1016/j.rse.2017.06.031>
- 761 Gras, J.L., Jensen, J.B., 1999. Some Optical Properties of Smoke Aerosol in Indonesia. *Geophys.*  
762 *Res. Lett.* 26, 1393–1396.
- 763 Hall, J. V., Loboda, T. V., Giglio, L., McCarty, G.W., 2016. A MODIS-based burned area  
764 assessment for Russian croplands: Mapping requirements and challenges. *Remote Sens.*  
765 *Environ.* 184, 506–521. <https://doi.org/10.1016/j.rse.2016.07.022>

- 766 Harrison, M.E., Page, S.E., Limin, S.H., 2009. The global impact of Indonesian forest fires.  
767 *Biologist* 56, 156–163.
- 768 Hawbaker, T.J., Vanderhoof, M.K., Beal, Y.-J., Takacs, J.D., Schmidt, G.L., Falgout, J.T.,  
769 Williams, B., Fairaux, N.M., Caldwell, M.K., Picotte, J.J., Howard, S.M., Stitt, S., Dwyer,  
770 J.L., 2017. Mapping burned areas using dense time-series of Landsat data. *Remote Sens.*  
771 *Environ.* 198, 504–522. <https://doi.org/10.1016/j.rse.2017.06.027>
- 772 Hayasaka, H., Noguchi, I., Putra, E.I., Yulianti, N., Vadrevu, K., 2014. Peat-fire-related air  
773 pollution in Central Kalimantan, Indonesia. *Environ. Pollut.* 195, 257–266.  
774 <https://doi.org/10.1016/j.envpol.2014.06.031>
- 775 Heil, A., Kaiser, J.W., van der Werf, G.R., Wooster, M.J., Schultz, M.G., van der Gon, H.D.,  
776 2010. Assessment of the Real-Time Fire Emissions (GFASv0) by MACC, ECMWF  
777 Technical Memo No. 626.
- 778 Heymann, J., Reuter, M., Buchwitz, M., Schneising, O., Bovensmann, H., Burrows, J.P.,  
779 Massart, S., Kaiser, J.W., Crisp, D., 2017. CO<sub>2</sub> emission of Indonesian fires in 2015  
780 estimated from satellite-derived atmospheric CO<sub>2</sub> concentrations. *Geophys. Res. Lett.* 44,  
781 1537–1544. <https://doi.org/10.1002/2016GL072042>
- 782 Hoelzemann, J.J., Schultz, M.G., Brasseur, G.P., Granier, C., Simon, M., 2004. Global Wildland  
783 Fire Emission Model (GWEM): Evaluating the use of global area burnt satellite data. *J.*  
784 *Geophys. Res. D Atmos.* 109. <https://doi.org/10.1029/2003JD003666>
- 785 Hoscilo, A., Page, S.E., Tansey, K.J., Rieley, J.O., 2011. Effect of repeated fires on land-cover  
786 change on peatland in southern Central Kalimantan, Indonesia, from 1973 to 2005. *Int. J.*  
787 *Wildl. Fire* 20, 578–588. <https://doi.org/10.1071/WF10029>
- 788 Ichoku, C., Ellison, L., 2014. Global top-down smoke-aerosol emissions estimation using  
789 satellite fire radiative power measurements. *Atmos. Chem. Phys.* 14, 6643–6667.  
790 <https://doi.org/10.5194/acp-14-6643-2014>
- 791 Kaiser, J.W., Heil, A., Andreae, M.O., Benedetti, A., Chubarova, N., Jones, L., Morcrette, J.J.,  
792 Razinger, M., Schultz, M.G., Suttie, M., van der Werf, G.R., 2012. Biomass burning  
793 emissions estimated with a global fire assimilation system based on observed fire radiative  
794 power. *Biogeosciences* 9, 527–554. <https://doi.org/10.5194/bg-9-527-2012>
- 795 Kasischke, E.S., Bruhwiler, L.P., 2002. Emissions of carbon dioxide, carbon monoxide, and  
796 methane from boreal forest fires in 1998. *J. Geophys. Res.* 108, 8146.  
797 <https://doi.org/10.1029/2001JD000461>
- 798 Kim, P.S., Jacob, D.J., Mickley, L.J., Koplitz, S.N., Marlier, M.E., DeFries, R.S., Myers, S.S.,  
799 Chew, B.N., Mao, Y.H., 2015. Sensitivity of population smoke exposure to fire locations in  
800 Equatorial Asia. *Atmos. Environ.* 102, 11–17.  
801 <https://doi.org/10.1016/j.atmosenv.2014.09.045>
- 802 Koplitz, S.N., Mickley, L.J., Marlier, M.E., Buonocore, J.J., Kim, P.S., Liu, T., Sulprizio, M.P.,  
803 DeFries, R.S., Jacob, D.J., Schwartz, J., Pongsiri, M., Myers, S.S., 2016. Public health  
804 impacts of the severe haze in Equatorial Asia in September–October 2015: demonstration of  
805 a new framework for informing fire management strategies to reduce downwind smoke  
806 exposure. *Environ. Res. Lett.* 11, 094023. <https://doi.org/10.1088/1748-9326/11/9/094023>
- 807 Koplitz, S.N., Nolte, C.G., Pouliot, G.A., Vukovich, J.M., Beidler, J., 2018. Influence of  
808 uncertainties in burned area estimates on modeled wildland fire PM<sub>2.5</sub> and ozone pollution

- 809 in the contiguous U.S. Atmos. Environ. 191, 328–339.  
810 <https://doi.org/10.1016/j.atmosenv.2018.08.020>
- 811 Li, F., Martin, M.V., Hantson, S., Andreae, M.O., Arneth, A., Lasslop, G., Yue, C., Bachelet, D.,  
812 Forrest, M., Kaiser, J.W., Kluzek, E., Liu, X., Melton, J.R., Ward, D.S., Darmenov, A.S.,  
813 Hickler, T., Ichoku, C., Magi, B.I., Sitch, S., van der Werf, G.R., Wiedinmyer, C., 2019.  
814 Historical (1700–2012) Global Multi-model Estimates of the Fire Emissions from the Fire  
815 Modeling Intercomparison Project (FireMIP). Atmos. Chem. Phys. Discuss.  
816 <https://doi.org/10.5194/acp-2019-37>
- 817 Liu, T., Marlier, M.E., Karambelas, A., Jain, M., Singh, S., Singh, M.K., Gautam, R., DeFries,  
818 R.S., 2019. Missing emissions from post-monsoon agricultural fires in northwestern India:  
819 regional limitations of MODIS burned area and active fire products. Environ. Res.  
820 Commun. 1, 011007. <https://doi.org/10.1088/2515-7620/ab056c>
- 821 Maasackers, J.D., Jacob, D.J., Sulprizio, M.P., Turner, A.J., Weitz, M., Wirth, T., Hight, C.,  
822 DeFigueiredo, M., Desai, M., Schmeltz, R., Hockstad, L., Bloom, A.A., Bowman, K.W.,  
823 Jeong, S., Fischer, M.L., 2016. Gridded National Inventory of U.S. Methane Emissions.  
824 Environ. Sci. Technol. 50, 13123–13133. <https://doi.org/10.1021/acs.est.6b02878>
- 825 Marlier, M.E., DeFries, R.S., Kim, P.S., Koplitz, S.N., Jacob, D.J., Mickley, L.J., Myers, S.S.,  
826 2015. Fire emissions and regional air quality impacts from fires in oil palm, timber, and  
827 logging concessions in Indonesia. Environ. Res. Lett. 10, 085005.  
828 <https://doi.org/10.1088/1748-9326/10/8/085005>
- 829 Marlier, M.E., Liu, T., Yu, K., Buonocore, J.J., Koplitz, S.N., DeFries, R.S., Mickley, L.J.,  
830 Jacob, D.J., Schwartz, J., Wardhana, B.S., Myers, S.S., 2019. Fires, Smoke Exposure, and  
831 Public Health: An Integrative Framework to Maximize Health Benefits from Peatland  
832 Restoration. GeoHealth. (accepted)
- 833 Olson, D.M., Dinerstein, E., Wikramanayake, E.D., Burgess, N.D., Powell, G.V.N., Underwood,  
834 E.C., D’amico, J.A., Itoua, I., Strand, H.E., Morrison, J.C., Loucks, C.J., Allnutt, T.F.,  
835 Ricketts, T.H., Kura, Y., Lamoreux, J.F., Wettengel, W.W., Hedao, P., Kassem, K.R., 2001.  
836 Terrestrial Ecoregions of the World: A New Map of Life on Earth. Bioscience 51, 933.  
837 [https://doi.org/10.1641/0006-3568\(2001\)051\[0933:TEOTWA\]2.0.CO;2](https://doi.org/10.1641/0006-3568(2001)051[0933:TEOTWA]2.0.CO;2)
- 838 Page, S., Hoscilo, A., Langner, A., Tansey, K., Siegert, F., Limin, S., Rieley, J., 2009. Tropical  
839 peatland fires in Southeast Asia, in: Tropical Fire Ecology: Climate Change, Land Use, and  
840 Ecosystem Dynamics. Springer Berlin Heidelberg, Berlin, Heidelberg, pp. 263–287.  
841 [https://doi.org/10.1007/978-3-540-77381-8\\_9](https://doi.org/10.1007/978-3-540-77381-8_9)
- 842 Prentice, I.C., Kelley, D.I., Foster, P.N., Friedlingstein, P., Harrison, S.P., Bartlein, P.J., 2011.  
843 Modeling fire and the terrestrial carbon balance. Global Biogeochem. Cycles 25, GB3005.  
844 <https://doi.org/10.1029/2010GB003906>
- 845 Randerson, J.T., Chen, Y., van der Werf, G.R., Rogers, B.M., Morton, D.C., 2012. Global  
846 burned area and biomass burning emissions from small fires. J. Geophys. Res.  
847 Biogeosciences 117, G04012. <https://doi.org/10.1029/2012JG002128>
- 848 Rein, G., Cleaver, N., Ashton, C., Pironi, P., Torero, J.L., 2008. The severity of smouldering peat  
849 fires and damage to the forest soil. Catena 74, 304–309.  
850 <https://doi.org/10.1016/j.catena.2008.05.008>
- 851 Rogers, B.M., Soja, A.J., Goulden, M.L., Randerson, J.T., 2015. Influence of tree species on

- 852 continental differences in boreal fires and climate feedbacks. *Nat. Geosci.* 8, 228–234.  
853 <https://doi.org/10.1038/ngeo2352>
- 854 Roteta, E., Bastarrika, A., Padilla, M., Storm, T., Chuvieco, E., 2019. Development of a Sentinel-  
855 2 burned area algorithm: Generation of a small fire database for sub-Saharan Africa.  
856 *Remote Sens. Environ.* 222, 1–17. <https://doi.org/10.1016/j.rse.2018.12.011>
- 857 Schroeder, W., Giglio, L., 2017. Visible Infrared Imaging Radiometer Suite (VIIRS) 375 m &  
858 750 m Active Fire Detection Data Sets Based on NASA VIIRS Land Science Investigator  
859 Processing System (SIPS) Reprocessed Data - Version 1.
- 860 Shi, Y., Matsunaga, T., Saito, M., Yamaguchi, Y., Chen, X., 2015. Comparison of global  
861 inventories of CO<sub>2</sub> emissions from biomass burning during 2002–2011 derived from  
862 multiple satellite products. *Environ. Pollut.* 206, 479–487.  
863 <https://doi.org/10.1016/j.envpol.2015.08.009>
- 864 Stockwell, C.E., Jayarathne, T., Cochrane, M.A., Ryan, K.C., Putra, E.I., Saharjo, B.H.,  
865 Nurhayati, A.D., Albar, I., Blake, D.R., Simpson, I.J., Stone, E.A., Yokelson, R.J., 2016.  
866 Field measurements of trace gases and aerosols emitted by peat fires in Central Kalimantan,  
867 Indonesia, during the 2015 El Niño. *Atmos. Chem. Phys.* 16, 11711–11732.  
868 <https://doi.org/10.5194/acp-16-11711-2016>
- 869 Sulla-Menashe, D., Gray, J.M., Abercrombie, S.P., Friedl, M.A., 2019. Hierarchical mapping of  
870 annual global land cover 2001 to present: The MODIS Collection 6 Land Cover product.  
871 *Remote Sens. Environ.* 222, 183–194. <https://doi.org/10.1016/j.rse.2018.12.013>
- 872 Tosca, M.G., Randerson, J.T., Zender, C.S., 2013. Global impact of smoke aerosols from  
873 landscape fires on climate and the Hadley circulation. *Atmos. Chem. Phys.* 13, 5227–5241.  
874 <https://doi.org/10.5194/acp-13-5227-2013>
- 875 van der Werf, G.R., Dempewolf, J., Trigg, S.N., Randerson, J.T., Kasibhatla, P.S., Giglio, L.,  
876 Murdiyarto, D., Peters, W., Morton, D.C., Collatz, G.J., Dolman, A.J., DeFries, R.S., 2008.  
877 Climate regulation of fire emissions and deforestation in equatorial Asia. *Proc. Natl. Acad.*  
878 *Sci.* 105, 20350–20355. <https://doi.org/10.1073/pnas.0803375105>
- 879 van der Werf, G.R., Randerson, J.T., Giglio, L., Collatz, G.J., Mu, M., Kasibhatla, P.S., Morton,  
880 D.C., Defries, R.S., Jin, Y., Van Leeuwen, T.T., 2010. Global fire emissions and the  
881 contribution of deforestation, savanna, forest, agricultural, and peat fires (1997–2009).  
882 *Atmos. Chem. Phys.* 10, 11707–11735. <https://doi.org/10.5194/acp-10-11707-2010>
- 883 van der Werf, G.R., Randerson, J.T., Giglio, L., van Leeuwen, T.T., Chen, Y., Rogers, B.M.,  
884 Mu, M., van Marle, M.J.E., Morton, D.C., Collatz, G.J., Yokelson, R.J., Kasibhatla, P.S.,  
885 2017. Global fire emissions estimates during 1997–2016. *Earth Syst. Sci. Data* 9, 697–720.  
886 <https://doi.org/10.5194/essd-9-697-2017>
- 887 Wiedinmyer, C., Akagi, S.K., Yokelson, R.J., Emmons, L.K., Orlando, J.J., Soja, A.J., 2011. The  
888 Fire INventory from NCAR (FINN): a high resolution global model to estimate the  
889 emissions from open burning. *Geosci. Model Dev.* 4, 625–641.  
890 <https://doi.org/10.5194/gmd-4-625-2011>
- 891 Wilson, A.M., Jetz, W., 2016. Remotely Sensed High-Resolution Global Cloud Dynamics for  
892 Predicting Ecosystem and Biodiversity Distributions. *PLoS Biol.* 14, 1–20.  
893 <https://doi.org/10.1371/journal.pbio.1002415>
- 894 Wooster, M.J., Roberts, G., Perry, G.L.W., Kaufman, Y.J., 2005. Retrieval of biomass

- 895 combustion rates and totals from fire radiative power observations: FRP derivation and  
896 calibration relationships between biomass consumption and fire radiative energy release. *J.*  
897 *Geophys. Res. Atmos.* 110, D24311. <https://doi.org/10.1029/2005JD006318>
- 898 Xiang, H., Liu, J., Cao, C., Xu, M., 2013. Algorithms for Moderate Resolution Imaging  
899 Spectroradiometer cloud-free image compositing. *J. Appl. Remote Sens.* 7, 073486.  
900 <https://doi.org/10.1117/1.JRS.7.073486>
- 901 Xu, J., Morris, P.J., Liu, J., Holden, J., 2018. PEATMAP: Refining estimates of global peatland  
902 distribution based on a meta-analysis. *Catena* 160, 134–140.  
903 <https://doi.org/10.1016/j.catena.2017.09.010>
- 904 Yi, Y., Kimball, J.S., Reichle, R.H., 2014. Spring hydrology determines summer net carbon  
905 uptake in northern ecosystems. *Environ. Res. Lett.* 9, 064003. [https://doi.org/10.1088/1748-](https://doi.org/10.1088/1748-9326/9/6/064003)  
906 [9326/9/6/064003](https://doi.org/10.1088/1748-9326/9/6/064003)
- 907 Zhang, F., Wang, J., Ichoku, C., Hyer, E.J., Yang, Z., Ge, C., Su, S., Zhang, X., Kondragunta, S.,  
908 Kaiser, J.W., Wiedinmyer, C., da Silva, A., 2014. Sensitivity of mesoscale modeling of  
909 smoke direct radiative effect to the emission inventory: A case study in northern sub-  
910 Saharan African region. *Environ. Res. Lett.* 9, 075002. [https://doi.org/10.1088/1748-](https://doi.org/10.1088/1748-9326/9/7/075002)  
911 [9326/9/7/075002](https://doi.org/10.1088/1748-9326/9/7/075002)
- 912 Zhang, T., Wooster, M.J., de Jong, M.C., Xu, W., 2018. How Well Does the “Small Fire Boost”  
913 Methodology Used within the GFED4.1s Fire Emissions Database Represent the Timing,  
914 Location and Magnitude of Agricultural Burning? *Remote Sens.* 10, 823.  
915 <https://doi.org/10.3390/rs10060823>
- 916

## 917 **List of Figure Captions**

918 **Table 1.** Comprehensive comparison of the global fire emissions inventories for various  
919 methodological details and technical parameters. Broadly, we define “bottom-up” as burned  
920 area-based and “top-down” as fire energy-based inventories.

921 **Figure 1. Metric 1 for relative fire confidence score ( $\phi_{area}$ ):** discrepancy between MCD64A1  
922 burned area (BA) and MxD14A1 active fire area (AFA) based on the normalized difference of  
923 BA outside AFA and AFA outside BA. Values are averaged over 2003-2017 and mapped at  
924  $0.25^\circ \times 0.25^\circ$  spatial resolution. High values (darker red) indicate relatively more confidence in  
925 BA than AFA, and low values (darker blue) the opposite.

926 **Figure 2. Metric 2 for relative fire confidence score ( $\phi_{cloud\_haze}$ ):** Cloud/haze fraction based  
927 on MxD09GA surface reflectance and weighted by FRP. Values are averaged 2003-2017 and  
928 mapped at  $0.25^\circ \times 0.25^\circ$  spatial resolution. High FRP-weighted cloud/haze fraction indicates  
929 fewer opportunities for satellite observation of the land surface during the fire season.

930 **Figure 3. Metric 3 for relative fire confidence score ( $\phi_{fragment}$ ):** average burned area ( $\text{km}^2$ )  
931 per “fragment,” or contiguous patch of burned area, averaged over 2003-2017 and mapped at  
932  $0.25^\circ \times 0.25^\circ$  spatial resolution. High values indicate dominance of large, contiguous fires; low  
933 values denote dominance of small, fragmented fires.

934 **Figure 4. Metric 4 for relative fire confidence score ( $\phi_{topography}$ ):** roughness in topography,  
935 expressed as variance in elevation ( $\text{m}^2$ ), averaged over 2003-2017 and mapped at  $0.25^\circ \times 0.25^\circ$   
936 spatial resolution. High values in topography variance indicate steep gradients in elevation, or  
937 mountainous terrain, whereas low values indicate relatively flat terrain.

938 **Figure 5. Metric 5 for relative fire confidence score ( $\phi_{VIIRS\_sf}$ ):** additional fires detected by  
939 VIIRS. Values are the areal fraction of VIIRS FRP occurring outside MODIS burned area and  
940 active fire pixel area, averaged over 2003-2017 and mapped at  $0.25^\circ \times 0.25^\circ$  spatial resolution. A  
941 value of 0 indicates that all VIIRS active fires overlap MODIS active fires, and a value of 1  
942 indicates the presence of VIIRS active fires but no MODIS burned area or active fire  
943 observations.

944 **Table 2.** Average annual global  $\text{CO}_2$ , CO,  $\text{CH}_4$ , organic carbon (OC), black carbon (BC) and fine  
945 particulate matter ( $\text{PM}_{2.5}$ ) emissions ( $\text{Tg yr}^{-1}$ ,  $\pm 1\sigma$ ) by inventory, from 2003-2016. The percent  
946 difference in emissions relative to GFEDv4s is in brackets. For each species, the inventory with  
947 the highest emissions is denoted in bold font. The coefficient of variation (CV; %) indicates the  
948 spread of values, normalized by the mean, across the five inventories.

949 **Figure 6. Mean annual OC + BC emissions ( $\text{Tg yr}^{-1}$ ,  $\pm 1\sigma$ ), over 2003-2016, from five global  
950 fire emissions inventories (GFEDv4s, FINNv1.5, GFASv1.2, QFEDv2.5r1, and FEERv1.0-  
951 G1.2) for the 14 GFEDv4s basis regions (Figure S12; van der Werf et al., 2017). Acronyms for  
952 the 14 basis regions are given in Figure S12. The fraction of OC emissions is denoted by darker  
953 shades, and that of BC emissions by lighter shades. Vertical bars show one standard deviation of  
954 the means over time. The coefficient of variation across inventories (CV, %) is shown for each  
955 region.**

956 **Table 3.** Average emissions factors (g species kg<sup>-1</sup> dry matter) for CO<sub>2</sub>, CO, CH<sub>4</sub>, OC, BC and  
957 PM<sub>2.5</sub>, weighted by fractional emissions over GFEDv4s land use and land cover (LULC). The  
958 coefficient of variation (CV; %) gives the variation, normalized by the mean, across inventories  
959 by species.

960 **Figure 7. Indonesia fires, smoke exposure in Singapore, and AOD in Equatorial Asia**  
961 **during July-October in 2006.** (a) Total organic carbon (OC) and black carbon (BC) emissions  
962 from GFASv1.2. Sum of OC+BC fire emissions over Indonesia is shown inset. (b) Sensitivity of  
963 mean July-October smoke concentrations in Singapore to the location of fire emissions,  
964 calculated by the GEOS-Chem adjoint. (c) Contribution of smoke PM<sub>2.5</sub> in Singapore from fires  
965 in individual grid cells over Indonesia, modeled using GFASv1.2 fire emissions. Average,  
966 calculated smoke PM<sub>2.5</sub> exposure in Singapore, which is the sum of these contributions, is shown  
967 inset. (d) Average MODIS Terra and Aqua aerosol optical depth (AOD) in Equatorial Asia. (e)  
968 Distribution of peatlands in Sumatra and Kalimantan, Indonesia. The approximate total peatland  
969 area in these regions is shown inset.

970 **Figure 8. Smoke PM<sub>2.5</sub> exposure in Singapore, from 2003-2016.** (a) Timeseries of monthly  
971 mean observed (black dots) and modeled (colored lines) smoke PM<sub>2.5</sub> concentrations. Observed  
972 smoke PM<sub>2.5</sub> is reconstructed from meteorological observations from the Singapore Changi  
973 Airport; only non-zero monthly smoke PM<sub>2.5</sub> observations are shown. Modeled values are from  
974 the GEOS-Chem adjoint using different global fire emissions inventories: GFEDv4s, FINNv1.5,  
975 GFASv1.2, QFEDv2.5r1, and FEERv1.0-G1.2. Correlations between observed and modeled  
976 smoke PM<sub>2.5</sub> are shown inset for each inventory and are statistically significant ( $p < 0.01$ ). (b)  
977 Jul-Oct mean smoke PM<sub>2.5</sub> by inventory, with observed smoke PM<sub>2.5</sub> indicated by dashed  
978 horizontal lines.

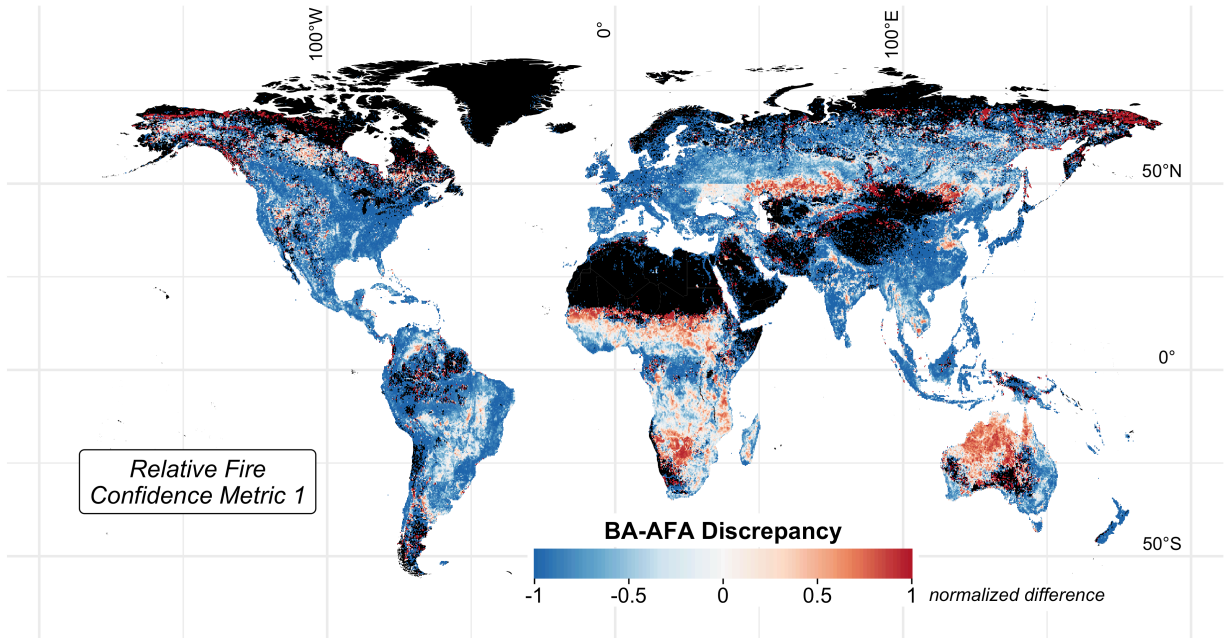
979 **Figure 9. Under-detection of 2015 Indonesia fires in MODIS active fire and burned area**  
980 **products relative to the 2003-2016 period.** CHIRPS rainfall rates (mm day<sup>-1</sup>) are plotted  
981 against MODIS (a) aerosol optical depth, (b) active fire count, (c) burned area (km<sup>2</sup>), and (d)  
982 FRP (GW) in log-log space. All variables are averaged temporally over July-October and  
983 spatially over Sumatra and Kalimantan, Indonesia. Colors denote different years from 2003-  
984 2016, with later years depicted by redder shades; values for 2015 are circled. Inset shows the  
985 correlation ( $r$ ,  $p < 0.01$ ), slope of the linear regression (gray dashed line), and slope with 2015  
986 removed (black line) for each pair of observations. Standard errors for the slopes are shown in  
987 parentheses. There is no statistically significant linear trend in any variable over time. Blue  
988 arrows in (b), (c), and (d) show that observed fires are lower than expected based on prediction  
989 from the linear regression of rainfall and fires that excludes 2015 observations. Percent  
990 underestimate of each fire variable based on these predictions is shown in blue.



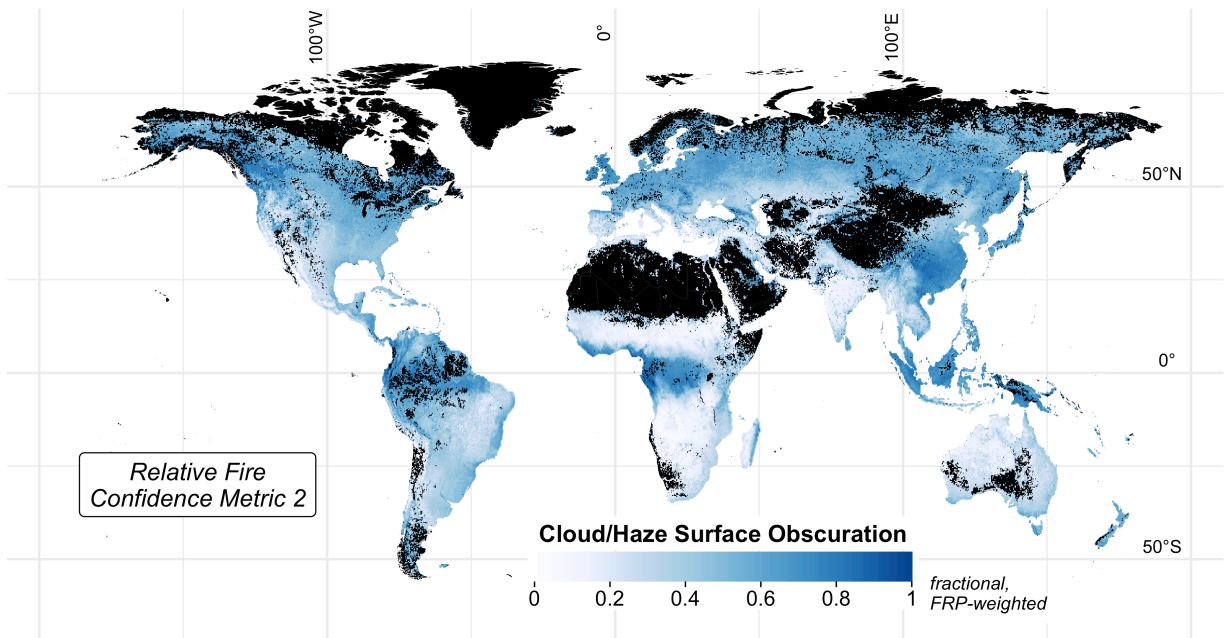
991 **Table 1.** Comprehensive comparison of the global fire emissions inventories for various  
 992 methodological details and technical parameters. Broadly, we define “bottom-up” as burned  
 993 area-based and “top-down” as fire energy-based inventories.

Inventory	GFEDv4s	FINNv1.5	GFASv1.2	QFEDv2.5r1	FEERv1.0-G1.2
	“Bottom-up”		“Top-down”		
Primary satellite fire input	MCD64A1 C5.1 burned area (500 m)	MCD14DL C5 active fire area (1 km)	MOD14/MYD14 C5/C6 FRP (1 km)	MOD14/MYD14 C6 FRP (1 km)	GFASv1.2 FRP (0.1°)
Spatio-temporal resolution	0.25°, monthly (daily fraction)	1 km, daily	0.1°, daily	0.1°, daily (0.25° x 0.375°, NRT)	0.1°, daily
Temporal range	1997-2018*	2002- (NRT)	2003- (NRT)	2000- (NRT)	2003- (NRT)
Statistical boosts	Small fires boost	x	Cloud gap adjustment		
Conversion to dry matter (DM) emissions	CASA biogeochemical model (van der Werf <i>et al.</i> , 2010)	Hoelzemann <i>et al.</i> (2004)	GFAS FRP-GFEDv3 DM conversion factors by LULC	QFED FRP-GFEDv2 DM global calibration	x
Smoke AOD constraints for aerosol emissions	x	x	Recommends 3.4 global scaling	Applies global scaling constants for OC, BC, PM <sub>2.5</sub> separately	Uses FRP-smoke AOD relationships to derive regional TPM emissions
Primary land use/land cover (LULC)	MCD12Q1 (UMD), annual (500 m)	MCD12Q1 (IGBP), 2005 (500 m)	GFEDv3 dominant fire-prone LULC (0.5°)	IGBP-INPE (1 km)	MODIS IGBP dominant fire-prone LULC, 2004 (1°)
Peatland maps	Olson <i>et al.</i> (2001)	x	Same as GFED3 Heil <i>et al.</i> (2010)	x	x
Partitioning of emissions by LULC	yes	yes	x	yes	x
Emissions factors	Akagi <i>et al.</i> (2011) + updates from M.O. Andreae in 2013	Akagi <i>et al.</i> (2011), Andreae & Merlet (2001)	Andreae and Merlet (2001) + updates from literature	Andreae and Merlet (2001)	Andreae and Merlet (2001) + updates from M.O. Andreae in 2014
Speciation	41 species	27 species	42 species	17 species	30 species
Ancillary products	boosted BA, diurnal cycle, NPP	x	cloud-gap adjusted FRP density, plume top/ smoke injection altitude	cloud-gap adjusted FRP density by LULC	x
References	van der Werf <i>et al.</i> (2017)	Wiedinmyer <i>et al.</i> (2011)	Kaiser <i>et al.</i> (2012)	Darmenov and da Silva (2013)	Ichoku and Ellison (2014)

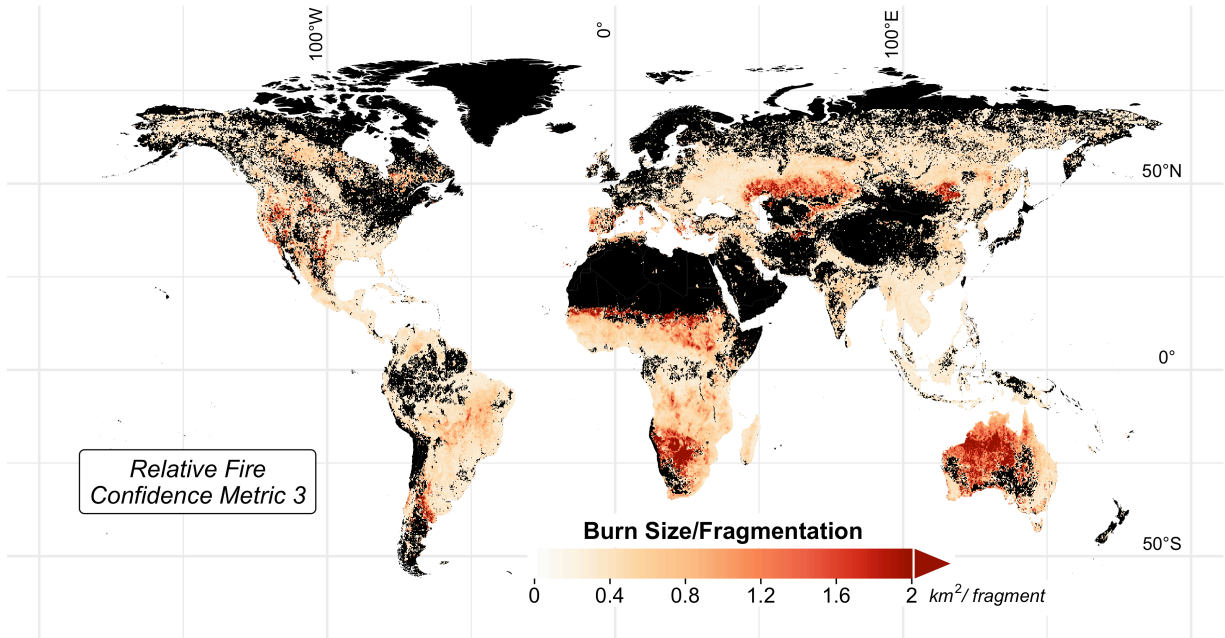
994 NRT = near real time; CASA = Carnegie Ames Stanford Approach; UMD = University of Maryland;  
 995 IGBP = International Biosphere-Geosphere Program; INPE = Instituto Nacional De Pesquisas Espaciais  
 996 (Brazil’s National Space Institute); NPP = Net Primary Production; \*2017-2018 are beta version releases



997  
998 **Figure 1. Metric 1 for relative fire confidence score ( $\phi_{area}$ ):** discrepancy between MCD64A1  
999 burned area (BA) and MxD14A1 active fire area (AFA) based on the normalized difference of  
1000 BA outside AFA and AFA outside BA. Values are averaged over 2003-2017 and mapped at  
1001 0.25° x 0.25° spatial resolution. High values (darker red) indicate relatively more confidence in  
1002 BA than AFA, and low values (darker blue) the opposite.

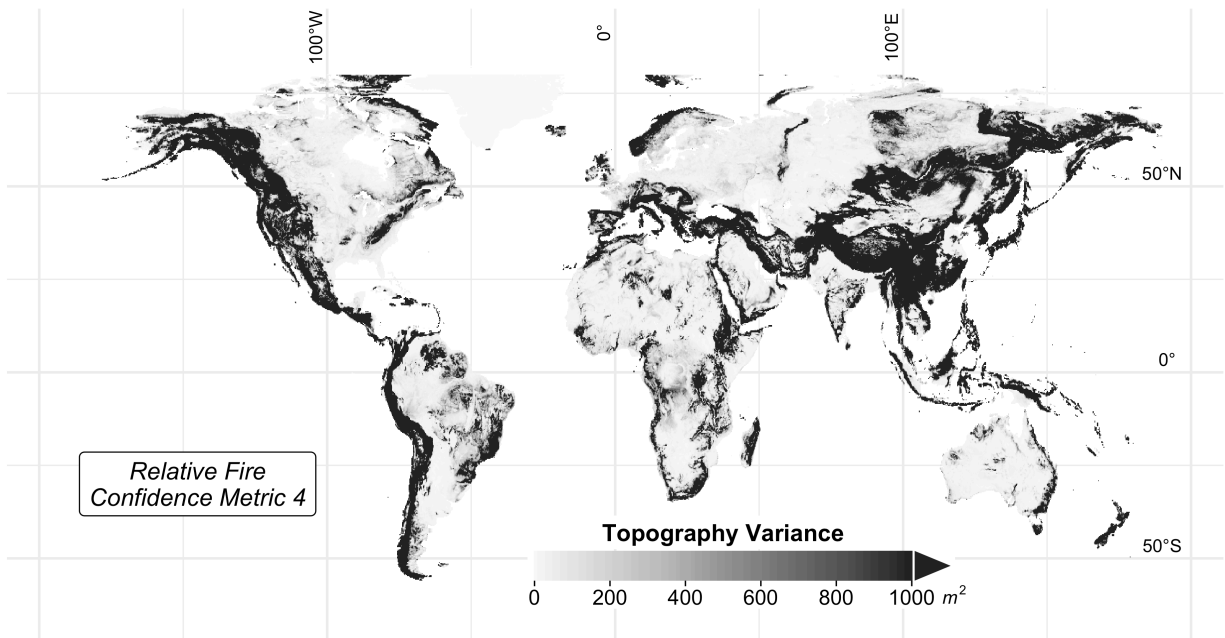


1003  
1004 **Figure 2. Metric 2 for relative fire confidence score ( $\phi_{cloud\_haze}$ ):** Cloud/haze fraction based  
1005 on MxD09GA surface reflectance and weighted by FRP. Values are averaged 2003-2017 and  
1006 mapped at 0.25° x 0.25° spatial resolution. High FRP-weighted cloud/haze fraction indicates  
1007 fewer opportunities for satellite observation of the land surface during the fire season.



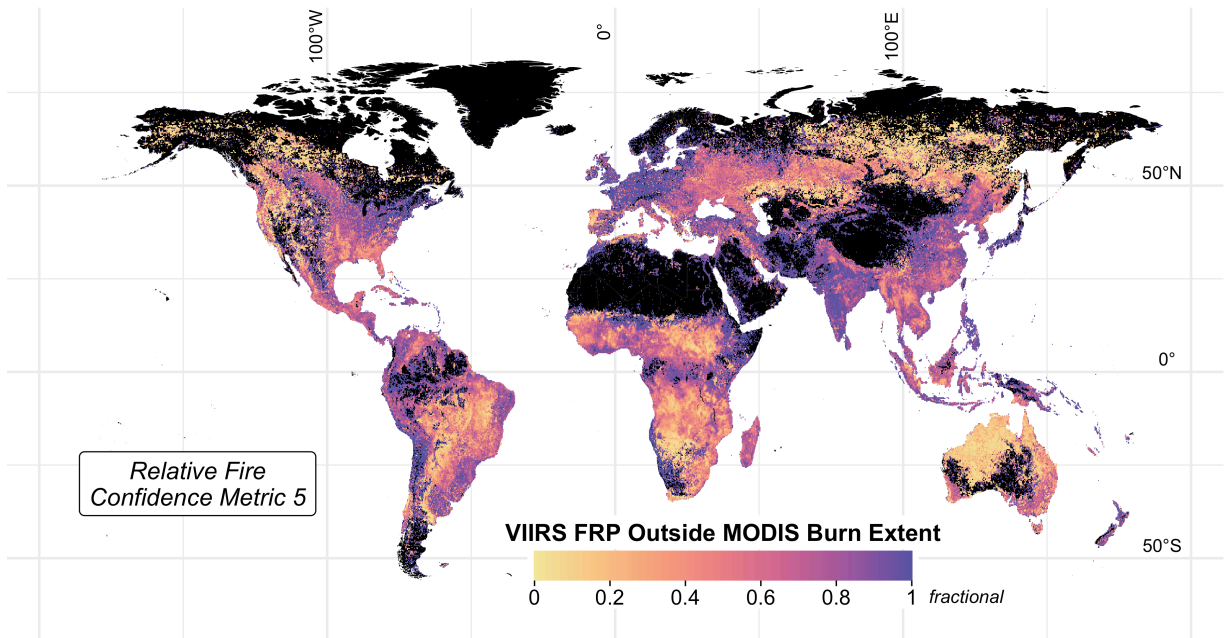
1008  
1009  
1010  
1011  
1012

**Figure 3. Metric 3 for relative fire confidence score ( $\phi_{fragment}$ ):** average burned area (km<sup>2</sup>) per “fragment,” or contiguous patch of burned area, averaged over 2003-2017 and mapped at 0.25° x 0.25° spatial resolution. High values indicate dominance of large, contiguous fires; low values denote dominance of small, fragmented fires.



1013  
1014  
1015  
1016  
1017

**Figure 4. Metric 4 for relative fire confidence score ( $\phi_{topography}$ ):** roughness in topography, expressed as variance in elevation (m<sup>2</sup>), averaged over 2003-2017 and mapped at 0.25° x 0.25° spatial resolution. High values in topography variance indicate steep gradients in elevation, or mountainous terrain, whereas low values indicate relatively flat terrain.



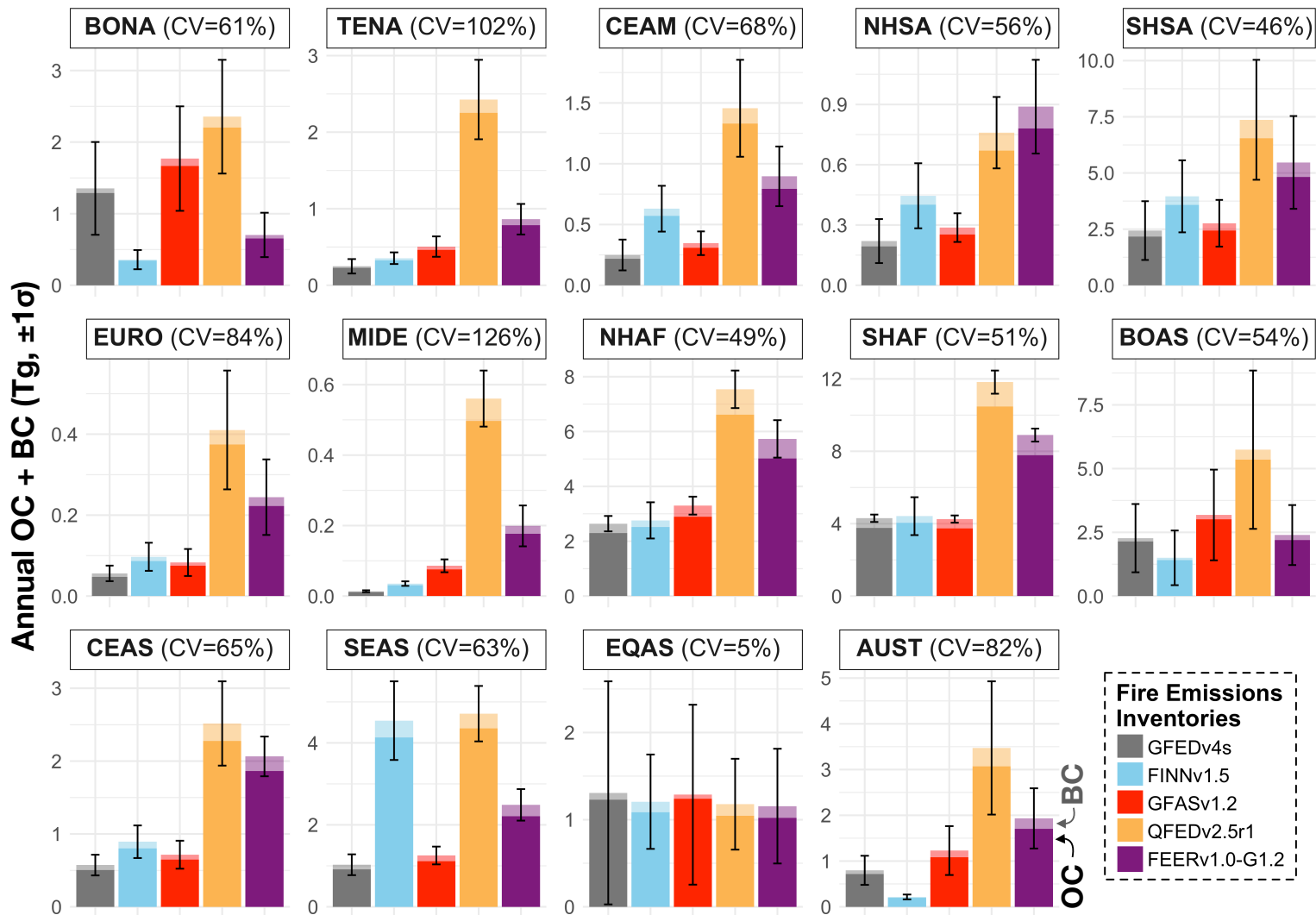
1018  
1019  
1020  
1021  
1022  
1023  
1024

**Figure 5. Metric 5 for relative fire confidence score ( $\phi_{VIIRS_{sf}}$ ):** additional fires detected by VIIRS. Values are the areal fraction of VIIRS FRP occurring outside MODIS burned area and active fire pixel area, averaged over 2003-2017 and mapped at 0.25° x 0.25° spatial resolution. A value of 0 indicates that all VIIRS active fires overlap MODIS active fires, and a value of 1 indicates the presence of VIIRS active fires but no MODIS burned area or active fire observations.

1025 **Table 2.** Average annual global CO<sub>2</sub>, CO, CH<sub>4</sub>, organic carbon (OC), black carbon (BC) and fine  
 1026 particulate matter (PM<sub>2.5</sub>) emissions (Tg yr<sup>-1</sup>, ±1σ) by inventory, from 2003-2016. The percent  
 1027 difference in emissions relative to GFEDv4s is in brackets. For each species, the inventory with  
 1028 the highest emissions is denoted in bold font. The coefficient of variation (CV; %) indicates the  
 1029 spread of values, normalized by the mean, across the five inventories.

Species	Mean Annual Global Emissions (Tg)					CV (%)
	<i>GFEDv4s</i>	<i>FINNv1.5</i>	<i>GFASv1.2</i>	<i>QFEDv2.5r1</i>	<i>FEERv1.0-G1.2</i>	
CO <sub>2</sub>	6986 (595) --	6292 (1137) [-10%]	7083 (604) [+1%]	7449 (665) [+7%]	<b>13205 (1044)</b> <b>[+89%]</b>	34
CO	336 (39) --	330 (60) [-2%]	366 (43) [+9%]	348 (31) [+4%]	<b>609 (52)</b> <b>[+81%]</b>	30
CH <sub>4</sub>	15 (3) --	16 (3) [+7%]	20 (3) [+35%]	15 (1) [+2%]	<b>30 (3)</b> <b>[+103%]</b>	34
OC	16 (2) --	20 (4) [+24%]	19 (2) [+21%]	<b>47 (5)</b> <b>[+199%]</b>	30 (3) [+91%]	49
BC	1.8 (0.2) --	1.9 (0.3) [+7%]	2.1 (0.2) [+15%]	<b>5.3 (0.5)</b> <b>[+196%]</b>	3.9 (0.3) [+119%]	52
PM <sub>2.5</sub>	35 (3) --	35 (6) [+1%]	31 (3) [-11%]	<b>74 (7)</b> <b>[+112%]</b>	51 (4) [+47%]	39

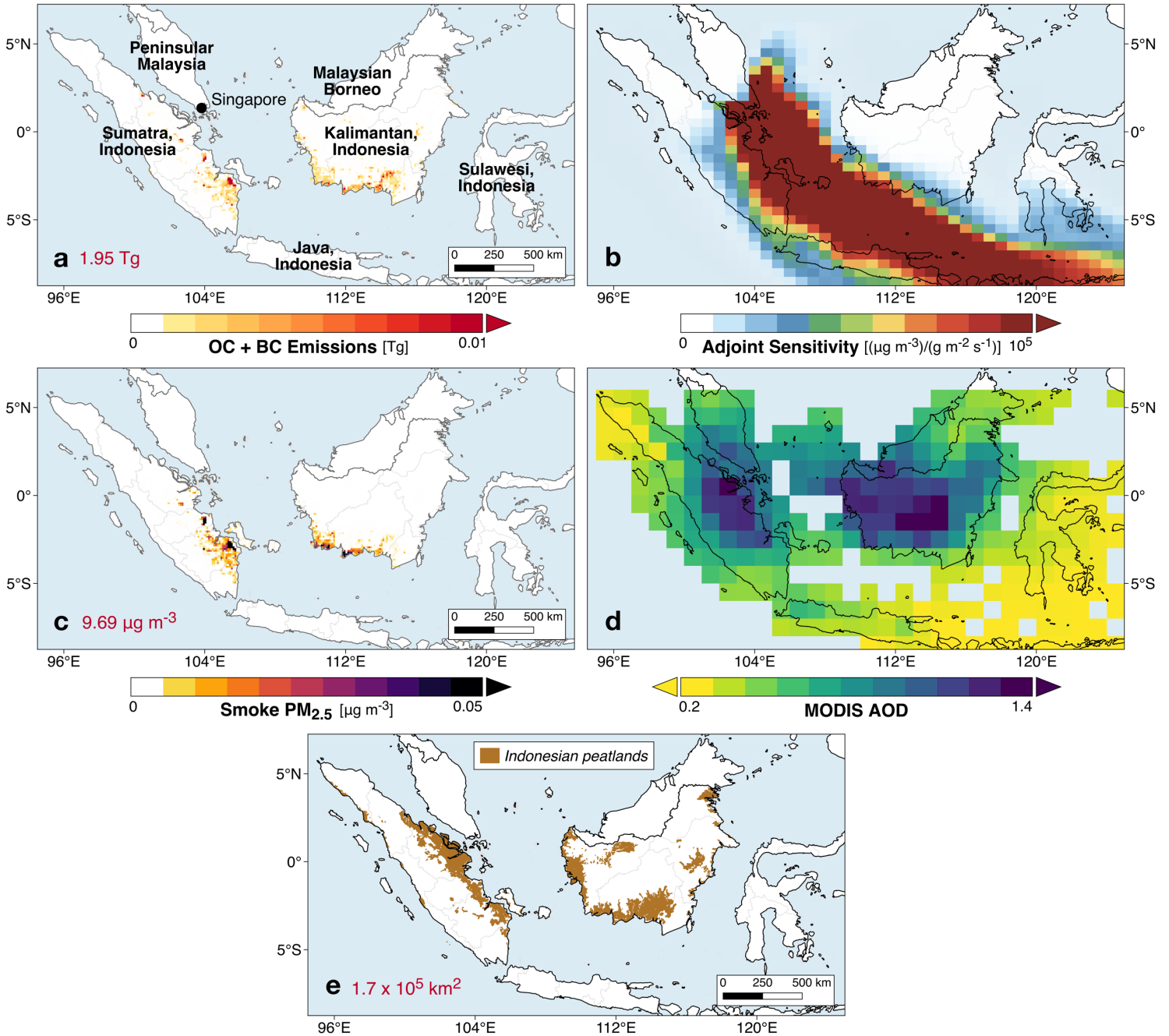
1030



1032 **Figure 6. Mean annual OC + BC emissions ( $Tg\ yr^{-1}, \pm 1\sigma$ ), over 2003-2016, from five global**  
 1033 **fire emissions inventories (GFEDv4s, FINNv1.5, GFASv1.2, QFEDv2.5r1, and FEERv1.0-**  
 1034 **G1.2) for the 14 GFEDv4s basis regions (Figure S12; van der Werf et al., 2017). Acronyms for**  
 1035 **the 14 basis regions are given in Figure S12. The fraction of OC emissions is denoted by darker**  
 1036 **shades, and that of BC emissions by lighter shades. Vertical bars show one standard deviation of**  
 1037 **the means over time. The coefficient of variation across inventories (CV, %) is shown for each**  
 1038 **region.**

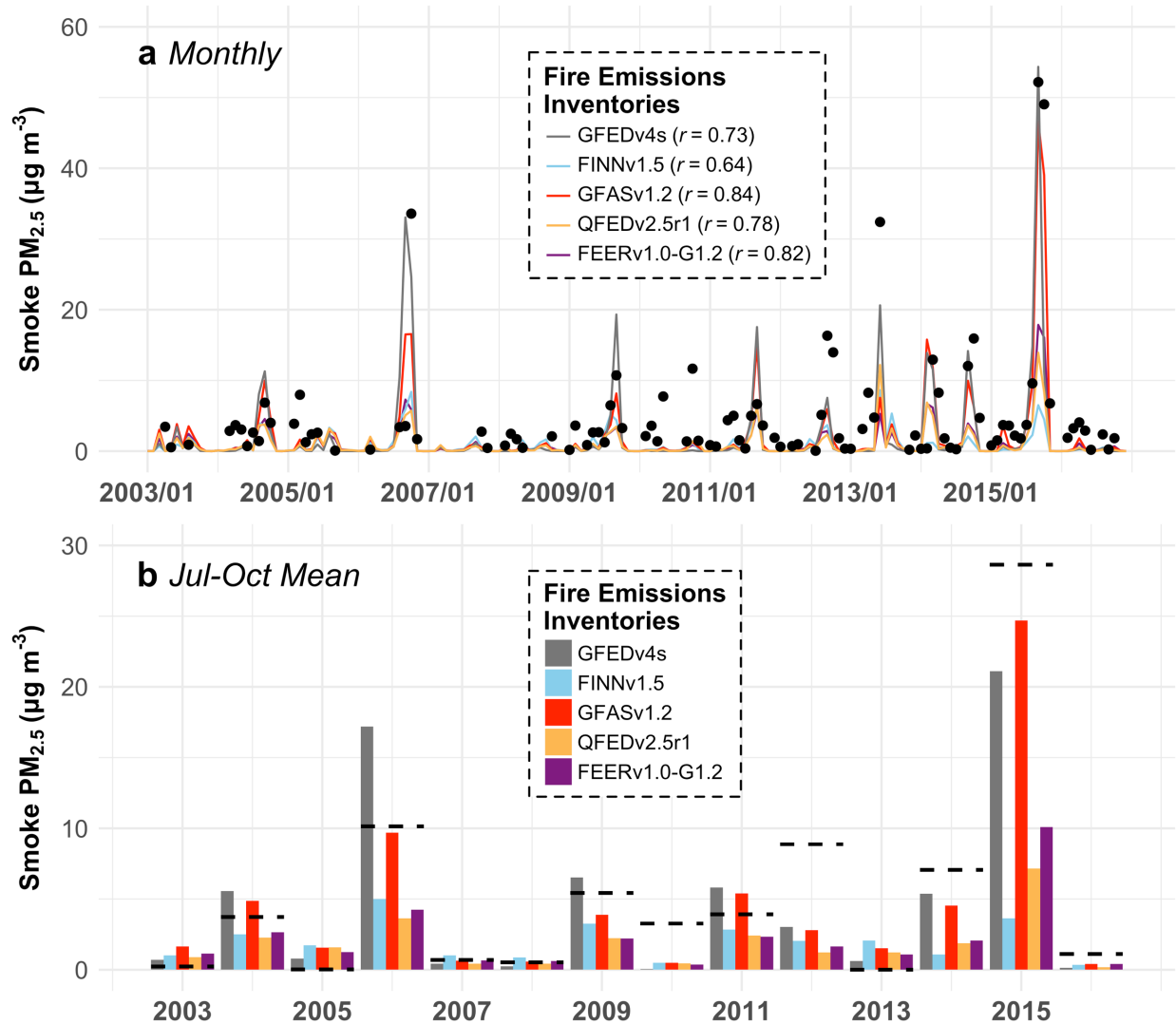
1039 **Table 3.** Average emissions factors (g species kg<sup>-1</sup> dry matter) for CO<sub>2</sub>, CO, CH<sub>4</sub>, OC, BC and  
 1040 PM<sub>2.5</sub>, weighted by fractional emissions over GFEDv4s land use and land cover (LULC). The  
 1041 coefficient of variation (CV; %) gives the variation, normalized by the mean, across inventories  
 1042 by species.

Species	Mean Emissions Factors (g species kg <sup>-1</sup> dry matter), Weighted by GFEDv4s LULC				CV (%)
	<i>GFEDv4s</i>	<i>FINNv1.0</i>	<i>GFASv1.0</i>	<i>QFEDv2.4</i>	
CO <sub>2</sub>	1648	1660	1611	1601	1.75
CO	95	87	91	84	5.45
CH <sub>4</sub>	6.67	4.43	7.1	4.2	26.7
OC	5.73	6.43	5.77	6.09	5.38
BC	0.47	0.46	0.49	0.53	6.67
PM <sub>2.5</sub>	9.65	12.46	8.29	8.29	20.3



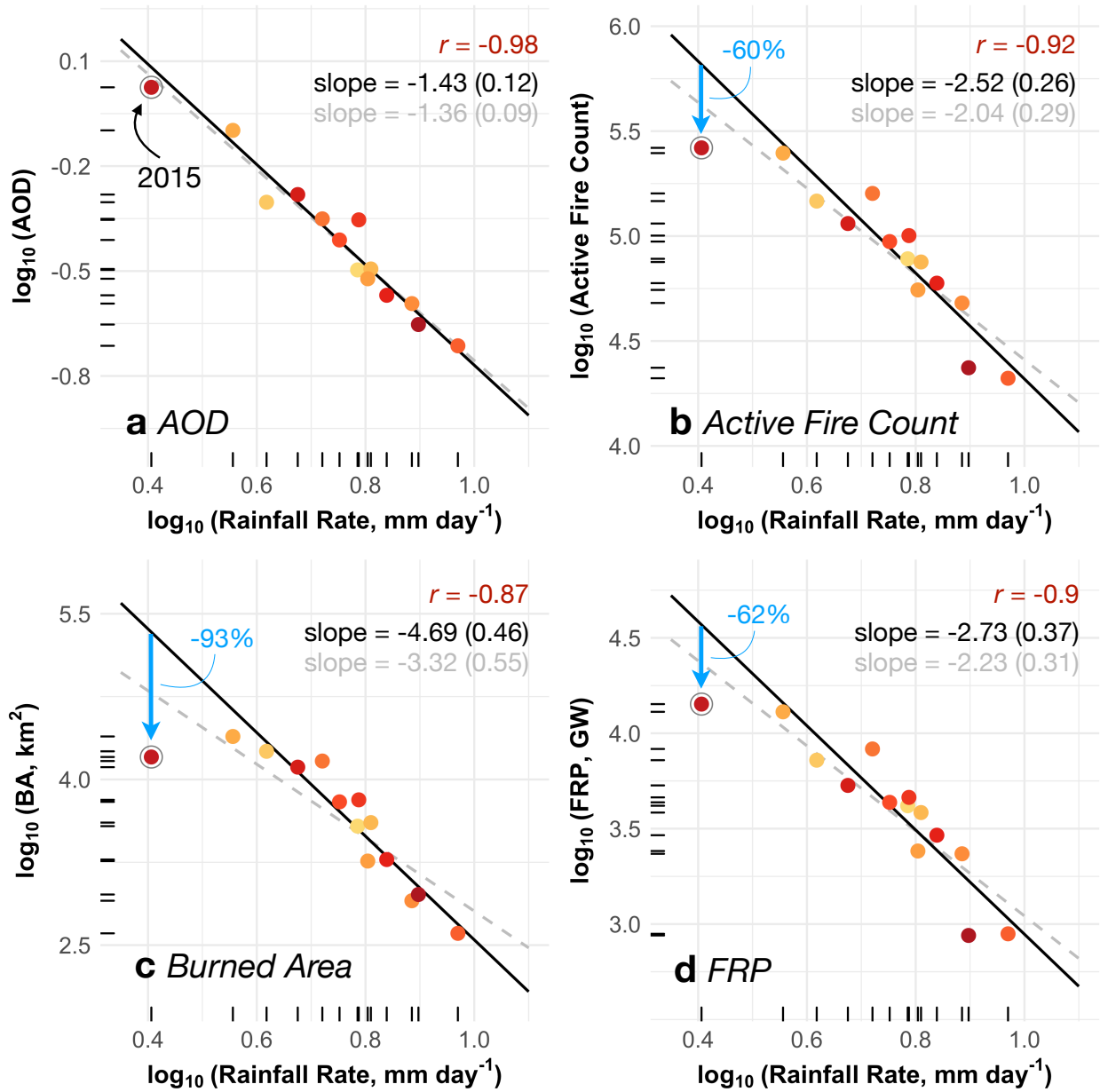
1044 **Figure 7. Indonesia fires, smoke exposure in Singapore, and AOD in Equatorial Asia**  
 1045 **during July-October in 2006. (a)** Total organic carbon (OC) and black carbon (BC) emissions  
 1046 from GFASv1.2. Sum of OC+BC fire emissions over Indonesia is shown inset. **(b)** Sensitivity of  
 1047 mean July-October smoke concentrations in Singapore to the location of fire emissions,  
 1048 calculated by the GEOS-Chem adjoint. **(c)** Contribution of smoke PM<sub>2.5</sub> in Singapore from fires  
 1049 in individual grid cells over Indonesia, modeled using GFASv1.2 fire emissions. Average,  
 1050 calculated smoke PM<sub>2.5</sub> exposure in Singapore, which is the sum of these contributions, is shown  
 1051 inset. **(d)** Average MODIS Terra and Aqua aerosol optical depth (AOD) in Equatorial Asia. **(e)**  
 1052 Distribution of peatlands in Sumatra and Kalimantan, Indonesia. The approximate total peatland  
 1053 area in these regions is shown inset.





1054

1055 **Figure 8. Smoke PM<sub>2.5</sub> exposure in Singapore, from 2003-2016.** (a) Timeseries of monthly  
1056 mean observed (black dots) and modeled (colored lines) smoke PM<sub>2.5</sub> concentrations. Observed  
1057 smoke PM<sub>2.5</sub> is reconstructed from meteorological observations from the Singapore Changi  
1058 Airport; only non-zero monthly smoke PM<sub>2.5</sub> observations are shown. Modeled values are from  
1059 the GEOS-Chem adjoint using different global fire emissions inventories: GFEDv4s, FINNv1.5,  
1060 GFASv1.2, QFEDv2.5r1, and FEERv1.0-G1.2. Correlations between observed and modeled  
1061 smoke PM<sub>2.5</sub> are shown inset for each inventory and are statistically significant ( $p < 0.01$ ). (b)  
1062 Jul-Oct mean smoke PM<sub>2.5</sub> by inventory, with observed smoke PM<sub>2.5</sub> indicated by dashed  
1063 horizontal lines.



1064

1065 **Figure 9. Under-detection of 2015 Indonesia fires in MODIS active fire and burned area**  
 1066 **products relative to the 2003-2016 period.** CHIRPS rainfall rates ( $\text{mm day}^{-1}$ ) are plotted  
 1067 against MODIS (a) aerosol optical depth, (b) active fire count, (c) burned area ( $\text{km}^2$ ), and (d)  
 1068 FRP (GW) in log-log space. All variables are averaged temporally over July-October and  
 1069 spatially over Sumatra and Kalimantan, Indonesia. Colors denote different years from 2003-  
 1070 2016, with later years depicted by redder shades; values for 2015 are circled. Inset shows the  
 1071 correlation ( $r$ ,  $p < 0.01$ ), slope of the linear regression (gray dashed line), and slope with 2015  
 1072 removed (black line) for each pair of observations. Standard errors for the slopes are shown in  
 1073 parentheses. There is no statistically significant linear trend in any variable over time. Blue  
 1074 arrows in (b), (c), and (d) show that observed fires are lower than expected based on prediction  
 1075 from the linear regression of rainfall and fires that excludes 2015 observations. Percent  
 1076 underestimate of each fire variable based on these predictions is shown in blue.